

# Climate-Invariant Machine Learning

Tom Beucler<sup>a,b,1</sup>, Michael Pritchard<sup>a</sup>, Janni Yuval<sup>c</sup>, Ankitesh Gupta<sup>a</sup>, Liran Peng<sup>a</sup>, Stephan Rasp<sup>d</sup>, Fiaz Ahmed<sup>e</sup>, Paul A. O’Gorman<sup>c</sup>, J. David Neelin<sup>e</sup>, Nicholas J. Lutsko<sup>f</sup>, and Pierre Gentine<sup>g</sup>

<sup>a</sup>Department of Earth System Science, University of California, Irvine, CA 92697, USA; <sup>b</sup>Institute of Earth Surface Dynamics, University of Lausanne, Lausanne, VD 1015, Switzerland; <sup>c</sup>Department of Earth, Atmospheric, and Planetary Sciences, Massachusetts Institute of Technology, Cambridge, MA 02139, USA; <sup>d</sup>Climate AI, San Francisco, CA 94111, USA; <sup>e</sup>Department of Atmospheric and Oceanic Sciences, University of California, Los Angeles, Los Angeles, CA 90095, USA; <sup>f</sup>Scripps Institution of Oceanography, University of California, San Diego, La Jolla, CA 92037, USA; <sup>g</sup>Department of Earth and Environmental Engineering, Columbia University, New York, NY 10027, USA

This manuscript was compiled on December 17, 2021

**Data-driven algorithms, in particular neural networks, can emulate the effects of unresolved processes in coarse-resolution climate models when trained on high-resolution simulation data; however, they often make large generalization errors when evaluated in conditions they were not trained on. Here, we propose to physically rescale the inputs and outputs of machine learning algorithms to help them generalize to unseen climates. Applied to offline parameterizations of subgrid-scale thermodynamics in three distinct climate models, we show that rescaled or “climate-invariant” neural networks make accurate predictions in test climates that are 4K and 8K warmer than their training climates. Additionally, “climate-invariant” neural nets facilitate generalization between Aquaplanet and Earth-like simulations. Through visualization and attribution methods, we show that compared to standard machine learning models, “climate-invariant” algorithms learn more local and robust relations between storm-scale convection, radiation, and their synoptic thermodynamic environment. Overall, these results suggest that explicitly incorporating physical knowledge into data-driven models of Earth system processes can improve their consistency and ability to generalize across climate regimes.**

Machine Learning | Climate Change | Earth System Science | Transfer Learning | Physics-Informed Machine Learning

Following its demonstrated success in computer vision and natural language processing, machine learning (ML<sup>\*</sup>) is rapidly percolating through climate science (e.g., reviews by 1–3). Examples include the emulation of radiative transfer (e.g., 4–7), gravity wave momentum fluxes (e.g., 8–10), and microphysical schemes (e.g., 11–13), the bias correction of climate predictions (e.g., 14, 15), the detection and classification of clouds and storms (e.g., 16–19), and the development of sub-grid closures from high-resolution simulation data (e.g., 20–22), which is the main application discussed in this manuscript.

While ML algorithms are typically designed to maximize accuracy on their training datasets, they make strong implicit assumptions when extrapolating outside of their training sets. To give common examples, multiple linear regressions (MLR) assume that the linear relationship that best describes the training set is universally valid. When confronted with out-of-distribution inputs, random forests (RF, 23) find the closest inputs in their training sets and assign the corresponding outputs regardless of the value of these out-of-distribution inputs. Neural networks (NN), which are powerful nonlinear regression and classification tools, rely on their nonlinear activation functions and fitted weights to extrapolate. Except in specific situations (e.g., out-of-distribution samples in the close neighborhood of the training set or described by the same nonlinear mapping as the training set), there is no reason why

NNs should generalize well far outside of their training sets.

In climate applications, this means that ML algorithms typically fail when exposed to dynamic or thermodynamic conditions that differ substantially from the range of conditions they were trained on, which remains under-reported in the research literature. Exceptions include (24), who showed that an RF-based moist convection scheme generalizes poorly in the tropics of a climate 6.5K warmer than the training climate although it could generalize well to a colder climate; and (25), who showed that an NN-based thermodynamic subgrid closure generalizes well to climates 1-2K warmer than the training one, but makes large errors as soon as the test climate is 4K warmer than the training one. (26) confirmed that these generalization errors remain even when the NN subgrid closure is modified to enforce conservation laws to within machine precision. Interestingly, (27) found that convolutional NNs (28) trained to classify thunderstorms in high-resolution model outputs generalize well to a warmer climate representing the end of the twenty-first century following the RCP8.5 emission scenario (29). While this may be because classifying thunderstorms relies heavily on wind velocity inputs, whose distributions change only slightly under an RCP8.5 warming scenario, the authors noted that using two types of ML layers, namely batch normalization (BN, 30) followed by dropout (DP, 31), was key to this successful generalization.

BN and DP are two examples of a larger set of methods used by the ML community to help NNs generalize and avoid

## Significance Statement

Predicting climate change is inherently a generalization problem: we extrapolate observations from the recent past using physical models we believe hold across past, present, and future climates. Current climate models are based on fundamental physical equations but require representations of processes that occur at scales smaller than the model grid size. Recent machine learning (ML) algorithms hold promise to improve such representations, but tend to extrapolate poorly to climate regimes they were not trained on. To get the best of the physical and statistical worlds, we propose a new framework — termed “climate-invariant” ML — for incorporating physical knowledge of climate processes into ML algorithms and show that they can maintain high accuracy across a wide range of climates and geographies.

TB, MP, SR, and PG initially designed the research. TB, MP, JY, AG, and LP performed the research. All authors contributed new analytic tools. TB, MP, JY, AG, and FA analyzed data. All authors wrote the paper.

The authors have no conflicts of interest to declare. See SI A for code and data availability.

<sup>1</sup>To whom correspondence should be addressed. E-mail: tom.beucler@gmail.com

arXiv:2112.08440v1 [cs.LG] 14 Dec 2021

\*here broadly describing algorithms that learn a task from data without being explicitly programmed for that task

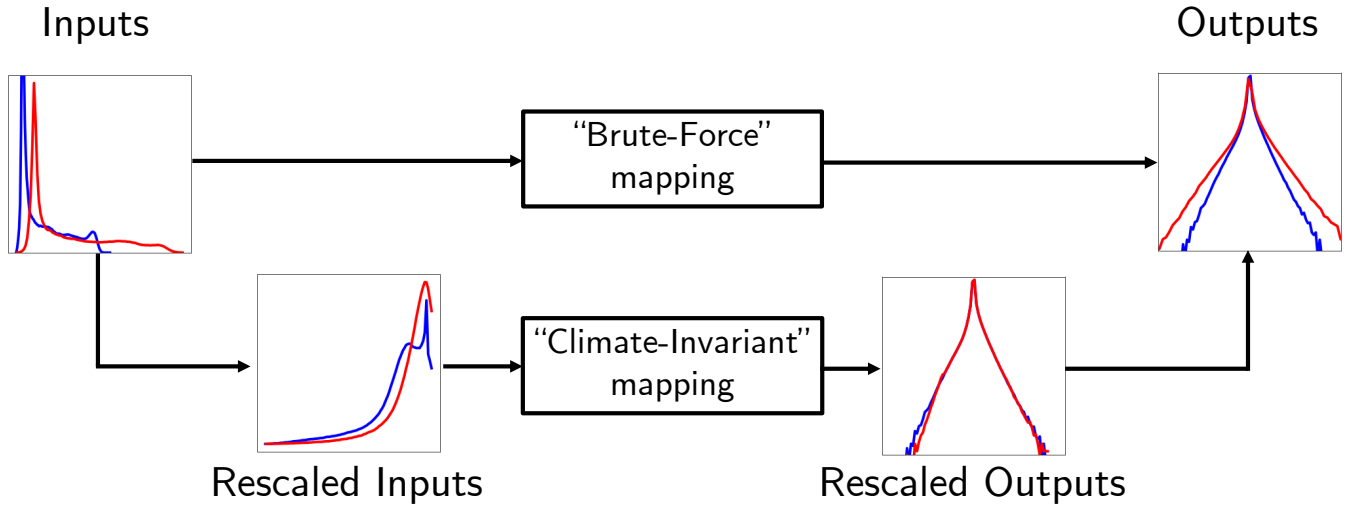


**Fig. 1.** By rescaling inputs and outputs to match their univariate PDFs across climates, algorithms can learn a mapping that holds across climates. To illustrate this, we show the PDFs of humidity-related inputs and outputs in two different climates using blue and red lines.

overfitting, broadly referred to as “regularization” (32). Most empirical regularization methods (e.g., L1 and L2 regularizations) rely on the principle of parsimony, i.e. that simpler models, accurately describing the training set with fewer fitted parameters, are preferable to more complex models and generalize better to unseen conditions. More systematic approaches to regularization have been developed in order to use ML models in out-of-distribution situations that still require the same inputs/outputs, referred to as domain adaptation (e.g., 33–35). However, most domain adaptation approaches (e.g., active, semi-supervised, and transductive learning) require at least a few samples in the generalization domain.

Here, we purposely focus on domain adaptation methods that do *not* require samples in the generalization domain for two reasons: (1) a long-term goal of the climate science community is to train ML models that rely only on observations and by definition we cannot observe the future climate; (2) even if we have access to simulation data across climates, ML models that generalize to climates they have not been trained on by construction are likely to be more robust to other changes (e.g., a change in model geography) as we will show in this manuscript. Motivated by this challenge, we ask:

How can we modify ML algorithms so that they make accurate predictions in climate conditions that – in standard variables – lie far outside of their training sets?

**Problem Definition.** Our main contribution is to transform the emulated mapping within the ML framework from a mapping that changes with climate, here referred to as “brute-force”, to a mapping that approximately remains constant across climates, here referred to as “climate-invariant”. Inspired by invariants in physics and self-similarity in fluid mechanics, we change the emulated mapping from “brute-force” to “climate-invariant” by rescaling the input and output vectors so that their distributions do not shift across climates (see Fig 1).

We demonstrate the utility of this framework by adapting several ML *closures of subgrid-scale atmospheric thermodynamics* (i.e., large-scale thermodynamic tendencies resulting from subgrid convection, radiation, and turbulence) so that they generalize better across climates. The motivation for

this application is two-fold. First, purely physically-based *subgrid closures* remain one of the largest sources of error in Earth system models (36–38). While ML-based closures have emerged as a promising alternative to traditional semi-empirical models (39), they lack robustness (40, 41) and, as discussed earlier, usually fail to generalize across climates (24–26). Second, *atmospheric thermodynamic processes* are directly affected by global temperature changes, e.g. in response to anthropogenically-forced climate change (42). Therefore, predicting subgrid thermodynamics in a warm climate with a ML model trained in a cold climate leads to very apparent failure modes (26) that we can transparently tackle.

In mathematical terms, our goal is to build a “climate-invariant” mapping between the input vector  $\mathbf{x}$  representing the large-scale ( $\approx 100\text{km}$ ) thermodynamic state:

$$\mathbf{x} = \left[ \mathbf{q}(p) \quad \mathbf{T}(p) \quad p_s \quad S_0 \quad \text{SHF} \quad \text{LHF} \right]^T, \quad [1]$$

and the output vector  $\mathbf{y}$  representing the large-scale thermodynamic tendencies due to explicitly-resolved convection and parameterized radiative transfer at the  $\sim 1\text{km}$ -scale, as well as parameterized turbulent mixing:

$$\mathbf{y} = \left[ L_v \dot{\mathbf{q}}(p) \quad c_p \dot{\mathbf{T}}(p) \quad c_p \mathbf{lw}(p) \quad c_p \mathbf{sw}(p) \right]^T, \quad [2]$$

where  $\mathbf{q}(p)$  is the vertical profile of specific humidity in units  $\text{kg}/\text{kg}$  (written as a function of the background pressure coordinate  $p$  in units Pa),  $\mathbf{T}(p)$  is the temperature’s vertical profile in units K,  $p_s$  is surface pressure in units Pa,  $S_0$  is solar insolation in units  $\text{W}/\text{m}^2$ , SHF is surface sensible heat flux in units  $\text{W}/\text{m}^2$ , LHF is surface latent heat flux in units  $\text{W}/\text{m}^2$ ,  $L_v \approx 2.50 \times 10^6 \text{J kg}^{-1}$  is the latent heat of vaporization of water in standard conditions,  $\dot{\mathbf{q}}(p)$  is the subgrid moistening vertical profile,  $c_p \approx 1.00 \times 10^3 \text{J kg}^{-1} \text{K}^{-1}$  is the specific heat of water at constant pressure in standard atmospheric conditions,  $\dot{\mathbf{T}}(p)$  is the total subgrid heating vertical profile,  $\mathbf{lw}(p)$  is the subgrid longwave radiative heating vertical profile, and  $\mathbf{sw}(p)$  is the subgrid shortwave radiative heating vertical profile. Following (43), all components of the output vector  $\mathbf{y}$

are mass-weighted and vertically integrated throughout each vertical layer to yield energy flux units ( $\text{W}/\text{m}^2$ ). Assuming vertical profiles have  $N_p$  vertical levels,  $\mathbf{x}$  is of length  $(2N_p + 4)$  and  $\mathbf{y}$  is of length  $4N_p$ . The details of  $\mathbf{x}$  and  $\mathbf{y}$  are somewhat different for the convection-permitting model SAM (see “Data” Section).

We keep the overall structure of the mapping  $\mathbf{x} \mapsto \mathbf{y}$  fixed throughout the manuscript and aim to predict  $\mathbf{y}$  as accurately as possible in training and generalization climates. Note that this mapping makes implicit assumptions based on successful past attempts (25, 44), including locality in horizontal space and time (outputs only depend on inputs in the same atmospheric column at the same time step) and determinism (only one possible output vector for a given input vector). For simplicity, we do not predict changes in cloud liquid water and ice and exclude cloud water and greenhouse gases other than water vapor from the input vector  $\mathbf{x}$ .

After introducing the climate simulations and training/validation/test split (“Data” Section), we define the “climate invariant” mapping and physical input/output rescalings (“Theory” Section), and demonstrate and explain their ability to generalize (“Results” Section) before concluding. We refer the reader to the Supplementary Information (SI) for data availability (SI A), additional derivations and descriptions of the physical rescalings (SI B), the implementation of our ML framework (SI C), and additional results (SI D).

## Data

To test the robustness of our framework across climate models, we use three climate models and experimental set-ups : super-parameterized aquaplanet simulations using the Super-Parameterized Community Atmosphere Model version 3.0 (SPCAM3), super-parameterized Earth-like simulations using the Super-Parameterized Community Atmosphere Model version 5 (SPCAM5), and quasi-global aquaplanet hypohydrostatic simulations using the the System for Atmospheric Modeling version 6.3 (SAM). SPCAM assumes a strict scale separation between the resolved and subgrid processes, making it an ideal testbed to unambiguously machine learn local subgrid closures (25, 45). In contrast, SAM does not assume scale separation as a global convection-permitting model, which is more realistic but requires carefully coarse-graining its high-resolution simulation output (46). For each climate model, we run three simulations with three different prescribed surface temperature distributions:

- (+0K) A reference simulation with a range of surface temperatures analogous to the present climate
- (-4K) A cold simulation with surface temperatures 4K cooler than the (+0K) simulations
- (+4K) A warm simulation with surface temperatures 4K warmer than the (+0K) simulations

with the exception of SAM for which only the (-4K) and (+0K) simulations are available. We summarize the characteristics of each simulation set in Tab S1 and refer the reader to Fig 2 for a visualization of surface temperatures in each model (Fig 2a) and snapshots of mid-tropospheric subgrid heating (Fig 2b).

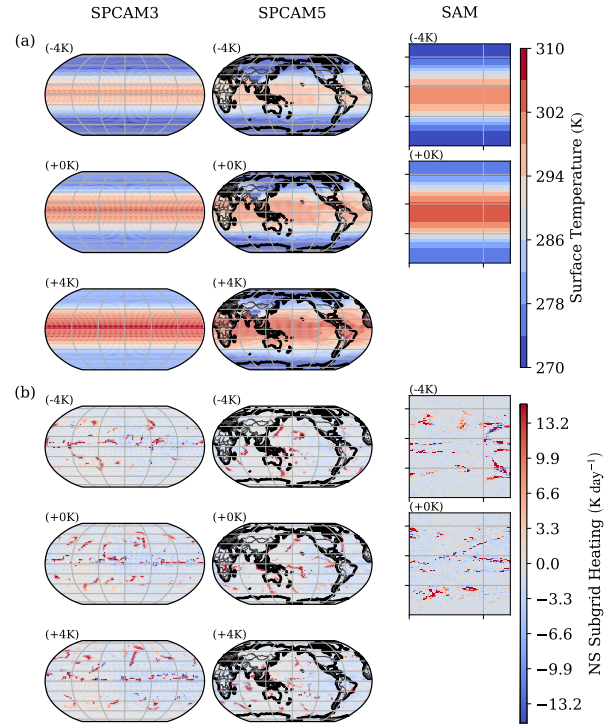


**Fig. 2.** (a) Prescribed surface temperature (in K) for (left) the aquaplanet SPCAM3 model and (right) the hypohydrostatic SAM model. (center) Annual-mean, near-surface air temperatures in the Earth-like SPCAM5 model. (b) Snapshots of near-surface subgrid heating rate (in K per day) for the same three models. For each model, we show the cold (-4K), reference (+0K), and warm (+4K) simulations.

**Super-Parameterized Aquaplanet Simulations.** We use two-year SPCAM3 (47) climate simulations in an aquaplanet configuration<sup>†</sup> (48), with zonally-symmetric surface temperatures fixed to a realistic meridionally-asymmetric profile (49). The insolation is fixed to boreal summer conditions with a full diurnal cycle. A two-dimensional convection-permitting model is embedded in each grid cell of SPCAM3, namely 8 SAM atmospheric columns, a spatiotemporal resolution of  $4\text{km} \times 30\text{lev} \times 25\text{s}$ , and the default one-moment microphysical scheme (50). The (+0K) SPCAM3 simulation was first presented in (45) and subsequently used to train ML subgrid closures in (25, 41, 43). Inspired by the generalization experiment of (24), the (+4K) simulation was introduced in (25), and we ran the (-4K) simulation for the work presented here to ambitiously increase the surface temperature generalization gap from 4K to 8K.

**Super-Parameterized Earth-like Simulations.** We run three two-year SPCAM5 (51) climate simulations in an Earth-like configuration, where the surface boundary conditions are realistic, including a land surface model, seasonality, aerosol conditions representative of the year 2000, and a zonally asymmetric annual climatology of sea surface temperatures derived from the “HadOIB1” dataset (52). We use the Community Earth Systems Model Version 2.1.3 to couple the Community Atmosphere Model Version 4.0 with the Community Land Model, and similarly embed 32 SAM columns in each atmospheric grid cell to explicitly represent deep convection. Our (+0K) simulation is almost identical to the Earth-like simula-

<sup>†</sup> an “ocean world” with no land



tion (44) recently used to show the potential of ML for subgrid closures in Earth-like conditions.

### Quasi-Global Aquaplanet Hypohydrostatic Simulations.

While super-parameterization is well-adapted to statistically learning subgrid closures thanks to its explicit scale separation, this scale separation comes at the cost of distorted mesoscale systems and momentum fluxes (53). Furthermore, most machine-learned subgrid closures are based on coarse-graining high-resolution simulations (e.g., 54, 55). This motivates us to test the “climate-invariant” framework in hypohydrostatic SAM simulations in which the dynamics are not affected by a scale separation. Computational expense is reduced through hypohydrostatic scaling which multiplies the vertical acceleration in the equations of motion by a factor of 16 to increase the horizontal scale of convection without overly affecting the larger-scale flow (56, 57). While these simulations use idealized settings, such as aquaplanet configurations, a quasi-global equatorial beta plane domain, and perpetual equinox without a diurnal cycle, (58) showed that they produce tropical rainfall intensity and cluster-area distributions that are close to satellite observations. The prescribed surface temperature distribution in the control simulation of (58) is designed to be close to zonal-mean observations (59), and its maximum value is roughly 2K colder than that of the distribution used for the 0K SPCAM3 simulation. To better match the SPCAM maxima of distributions of upper-level temperatures and humidities, we choose to treat this SAM control simulation as the (-4K) SAM simulation, and the warm simulation of (58) as the (+0K) SAM simulation. We refer the reader interested in the details of the simulations and the coarse-graining (here by a factor of 8) to (58) and the methods section of (46). We summarize key differences in the mappings that are learned for SAM as compared to SPCAM below:

- the input vector does not contain the specific humidity, surface pressure, sensible heat flux, or the latent heat flux, but instead contains the total water concentration and uses distance to the equator as a proxy for solar insolation,
- the output vector includes the subgrid total non-precipitating water tendency instead of the subgrid specific humidity tendency,
- the output vector does not contain the subgrid longwave and shortwave heating; instead the radiative heating is included in the temperature tendency  $\dot{T}$ ,
- SAM uses a height-based vertical coordinate rather than a pressure-based one, and
- the (+4K) SAM simulation is not available and so the generalization experiment is from the (-4K) to the (+0K) simulation.

**Training, Validation, and Test Split.** To understand which solutions have the most promise for helping ML algorithms generalize to unseen datasets, we purposely designed two difficult generalization experiments: (1) Training and validating ML models on cold simulations (-4K) and testing them on warm simulations (+4K); and (2) training and validating ML models on Aquaplanet simulations (SPCAM3) and testing

them on Earth-like simulations (SPCAM5). Both generalization experiments expose ML models to out-of-distribution inputs they have not been trained on. Following best ML practices, we used the *training* set to optimize the ML model’s free parameters, saved the free parameters that led to the best performance on the *validation* set to avoid overfitting the training set, and evaluated the final model on samples from a separate *test* set. We split each of the 9 simulations into training/validation/test sets by using separate 3-month periods (reported in Tab S1) to avoid high temporal correlations between training/validation/test set samples (60).

## Theory

We formally define a “*climate-invariant*” mapping as a mapping that is unchanged across climates. In practice, it is difficult, if not impossible, to find mappings that are exactly invariant and we will use the terminology “climate-invariant” for any mapping that remains approximately constant across climates. To achieve climate invariance, we introduce *physical rescalings*, defined as physically-informed functions that map the inputs/outputs to different inputs/outputs whose distributions vary less across climates. We deem the physical rescalings to be “climate-invariant” if they are so successful that the distributions of the inputs/outputs vary minimally across climates. Note that “climate-invariant” rescalings are distinct from dimensional analysis in fluid mechanics, as dimensional analysis does not necessarily affect distributions while “climate-invariant” rescalings may yield variables that are not dimensionless.

After introducing a workflow for identifying climate-invariant rescalings, we compare different possible input rescalings. We discuss output rescalings in SI B2 and possible vertical coordinate rescalings in SI B3.

**Finding Climate-Invariant Rescalings.** Fig 3 illustrates our proposed workflow for finding robust inputs/outputs rescalings that transform the initial “brute-force” mapping into a “climate-invariant” mapping when combined. Note that this workflow assumes that we cannot or do not want to retrain ML algorithms in the target climate, which excludes automatically finding a rescaling by training a model. This limitation could arise because the data in the target climate are insufficient or less reliable, or because we seek to uncover new physical relations that hold across an even wider range of climates.

The first step is to propose a physical rescaling to implement. We can do this through knowledge of robust physical or statistical relations that link and/or preserve distributions (e.g., state equations, self-similarities, conservation laws, accurate empirical relations, etc). These relations help derive invariants (e.g., 61) under a change in thermodynamic conditions. Before taking the time to implement this rescaling in the ML workflow, we can verify that the PDFs of the rescaled inputs/outputs match in the training and target climates. Ideally, the joint PDFs of the rescaled inputs/outputs would perfectly match. In practice, because it is easier to rescale one variable at a time and the data are often insufficient in the target climate, we can fall back on the necessary (but not sufficient) condition that the univariate PDFs of the rescaled inputs/outputs must match in the training and target climates. Mathematically, this match can be quantified using PDF distance metrics.

An additional challenge is that the original and rescaled



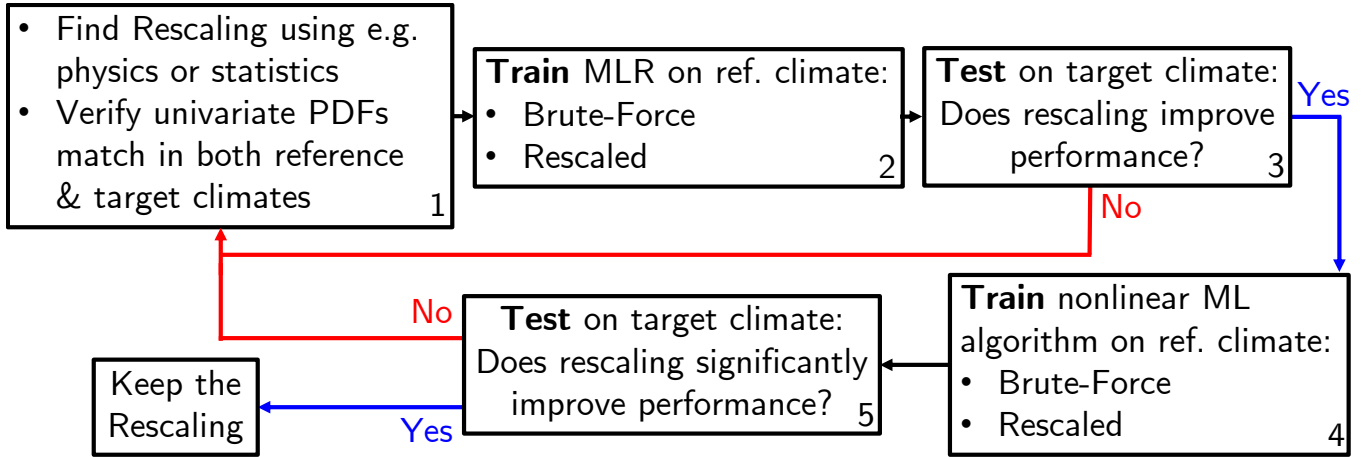


**Fig. 3.** Proposed five-step workflow to find climate-invariant rescalings that help Machine Learning (ML) models generalize from a reference (ref.) climate to a target one, using (top) a baseline Multiple Linear Regression (MLR) as an initial guide.

variables may have different units and range, meaning that any nonlinear distance metric will complicate the PDF comparison. To address this, we normalize the PDFs and their support variables  $X$  so that the PDFs’ domains strictly lie within  $[0, 1]$ . For a given variable, we use the same normalization factors across climates:

$$X_{\text{norm}} \stackrel{\text{def}}{=} \frac{X - \min_{\text{cl}} X}{\max_{\text{cl}} X - \min_{\text{cl}} X}, \quad [3]$$

$$\text{PDF}_{\text{norm}} \stackrel{\text{def}}{=} \frac{\text{PDF}}{\int_0^1 dX_{\text{norm}} \times \text{PDF}(X_{\text{norm}})}, \quad [4]$$

where  $\text{PDF}_{\text{norm}}$  is the rescaled PDF and  $X_{\text{norm}}$  is its rescaled support, and  $\max_{\text{cl}}$  and  $\min_{\text{cl}}$  respectively refer to the maximum and minimum operators over the variables’ domains and across climates, i.e. over the (-4K), (+0K), and (+4K) simulations.

Once the PDFs of each variable are normalized, we may pick any informative PDF distance metric to quantify how PDFs match across climates. Here, we pick the commonly-used Hellinger distance between two PDFs  $p$  and  $q$ , formally defined (62) as:

$$\mathcal{H}(p, q) \stackrel{\text{def}}{=} \sqrt{\int_0^1 \frac{dx}{2} \left[ \sqrt{p(x)} - \sqrt{q(x)} \right]^2}. \quad [5]$$

This distance is symmetric (i.e., the arguments’ order does not affect the outcome) and easy to interpret:  $\mathcal{H}(p, q)$  is bounded by 0 (when  $p = q$ ) and 100% (when  $p$  is zero whenever  $q$  is positive and vice-versa). In SI D1, we show that our results using the Hellinger distance (see Tab 1) are consistent with those using the Jensen-Shannon distance (63), a PDF distance metric giving large weights to the PDFs’ tails that tend to be particularly problematic for generalization purposes.

Once the univariate PDFs of the physically rescaled variables match across climates, the second step is to train two inexpensive or “baseline” models<sup>‡</sup> on the reference climate to quickly check whether the rescaling improves an ML model’s generalization ability: (1) A “brute-force” model without the

<sup>‡</sup>Because we here develop climate-invariant *neural nets*, we suggest training *MLR* baselines, but note that the ML model used to define the baseline should be tailored to the desired final ML model.

Row	Input	SPCAM3	SPCAM5	SAM
1	$q_{600\text{hPa}}$	20.3, <b>35.1</b>	17.1, <b>29.5</b>	22.1
2	$q_{\text{deficit}, 600\text{hPa}}$	24.9, <b>36.5</b>	18.1, <b>31.0</b>	30.0
3	$\text{RH}_{600\text{hPa}}$	3.6, <b>8.2</b>	3.2, <b>5.3</b>	4.3
4	$T_{850\text{hPa}}$	53.2, <b>64.3</b>	25.7, <b>37.3</b>	51.9
5	$T_{\text{from NS}, 850\text{hPa}}$	5.1, <b>6.2</b>	3.3, <b>6.4</b>	10.5
6	$B_{\text{plume}, 850\text{hPa}}$	9.4, <b>14.7</b>	3.6, <b>7.6</b>	5.8
7	$T_{150\text{hPa}}$	30.2, <b>33.5</b>	31.6, <b>34.4</b>	65.6
8	$T_{\text{from NS}, 150\text{hPa}}$	38.0, <b>53.7</b>	14.5, <b>28.7</b>	51.0
9	$B_{\text{plume}, 150\text{hPa}}$	35.1, <b>42.2</b>	10.4, <b>20.9</b>	21.1
10	LHF	8.6, <b>14.5</b>	9.7, <b>12.5</b>	
11	$\text{LHF}_q$	4.7, <b>9.5</b>	10.0, <b>10.7</b>	
12	$\text{LHF}_{\Delta q}$	6.3, <b>9.9</b>	9.9, <b>14.0</b>	

**Table 1.** Hellinger distance (in %) away from the (-4K) simulation for the PDFs of ( $q_{600\text{hPa}}$ ,  $T_{850\text{hPa}}$ ,  $T_{150\text{hPa}}$ , LHF) and their rescalings: (+0K) distance in gray and (+4K) distance in red.

rescaling; and (2) a “climate-invariant” model with the rescaling. If the rescaling does not improve the baseline model’s generalization abilities (i.e., (2) performs worse than (1) in the target climate), then the rescaling may not be appropriate.

If the rescaling improves the inexpensive baseline model’s performances, the last step is to train the “brute-force” and “climate-invariant” versions of the desired ML model (usually nonlinear) on the reference climate. If the physical rescaling improves the desired ML model’s generalization abilities (i.e., the climate-invariant model beats the brute-force model in the target climate using the same performance metric), then we may keep the rescaling. This workflow may be repeated for the ML model’s additional input/output variables until the emulated mapping is as “climate-invariant” as possible.

Before applying this workflow to subgrid thermodynamics closures, we underline one of its key challenges: Because some rescalings are much more impactful than others, it is often not possible to develop each physical rescaling independently. In our case, the specific humidity inputs vary the most across climates, meaning that rescaling specific humidity affects the model’s generalization abilities the most. As a result, initial experiments that independently tested the effect of rescaling temperature suggested a negative impact of temperature rescaling on generalization ability (not shown). This initial re-

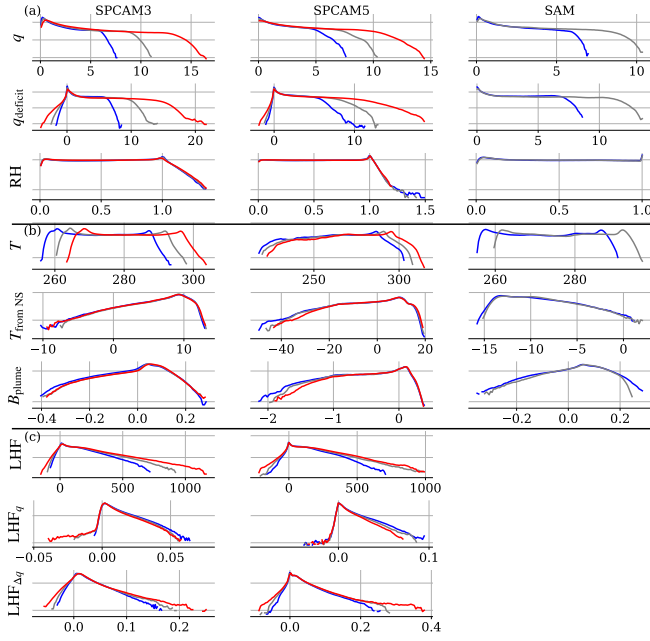


**Fig. 4.** Univariate PDFs of the (a) 600hPa specific humidity, (b) 850hPa temperature, and (c) latent heat flux in the cold (blue), reference (gray), and warm (red) simulations of each model (SPCAM3, SPCAM5, and SAM). For each variable, we also show the PDFs of the two rescalings discussed in the “Theory” section. From top to bottom, the variables are  $q$  (g/kg),  $q_{\text{deficit}}$  (g/kg), RH,  $T$  (K),  $T_{\text{from NS}}$  (K),  $B_{\text{plume}}$  ( $\text{m}^2/\text{s}^2$ ), LHF ( $\text{W}/\text{m}^2$ ),  $\text{LHF}_q$  ( $\text{kg m}^{-2}\text{s}^{-1}$ ), and  $\text{LHF}_{\Delta q}$  ( $\text{kg m}^{-2}\text{s}^{-1}$ ). For a given variable and rescaling, we use the same vertical logarithmic scale across models.

sult was later invalidated by experiments that jointly rescaled specific humidity and temperature (see below). Following this, we adopt a progressive input rescaling approach, where the most important inputs are rescaled first: Specific humidity, then temperature, and finally surface energy fluxes.

**Input Rescaling.** Throughout the following section, we compare three options for each input, whose univariate PDFs are depicted for all three climate models in Fig 4: No rescaling (top), our most successful rescaling (bottom), and our second best rescaling (middle).

**Specific Humidity.** Without any rescaling, the PDF of specific humidity  $q$  (Fig 4a, top) extends through a considerably larger range as the climate warms (Tab 1, row 1). This is because  $q$ 's upper bound, namely the saturation specific humidity  $q_{\text{sat}}(T, p)$ , increases quasi-exponentially with temperature through the Clausius-Clapeyron relation (e.g., 64, 65). Saturation deficit (Fig 4a, middle), defined as the amount by which the water vapor concentration must be increased to achieve saturation without changing the environmental temperature and pressure:

$$\tilde{q}_{\text{deficit}}(T, p) \stackrel{\text{def}}{=} q_{\text{sat}}(T, p) - q, \quad [6]$$

still has a corresponding expansion of the PDF with warming as a result of the Clausius-Clapeyron relation (Tab 1, row 2). In contrast, the relative humidity rescaling (Fig 4a, bottom):

$$\tilde{\text{RH}}(p) \stackrel{\text{def}}{=} \text{RH}(q, T, p) \quad [7]$$

normalizes specific humidity by its saturation value. As a result, most of the RH PDF lies within  $[0, 1]$ , except for a few

atmospheric columns exhibiting super-saturation in SPCAM, and that PDF changes little as the climate warms (Tab 1, row 3). In addition to capturing grid-scale saturation,  $\tilde{q}_{\text{RH}}$  helps predict the subgrid-scale effects of dry-air entrainment, known to regulate tropical convection (66–68) (See SI B1a for details of RH and saturation specific humidity calculations).

**Temperature.** As expected, the PDF of temperature  $T$  (Fig 4b, top) shifts quasi-linearly as the climate warms (Tab 1, row 4). Assuming that this shift is almost uniform with height, we can derive an (approximate) invariant by subtracting the temperature at all levels  $T(p)$  from the near-surface temperature  $T(p_{\text{NS}})$  (Fig 4b, middle):

$$\tilde{T}_{\text{from NS}}(p) \stackrel{\text{def}}{=} T(p_{\text{NS}}) - T(p), \quad [8]$$

where  $p_{\text{NS}}$  is the lowest atmospheric pressure level (Tab 1, row 5).

However, this linear rescaling fails in the upper atmosphere, especially near the tropopause where temperatures are approximately invariant with warming (69–71) and therefore decoupled from surface temperature changes (Tab 1, row 8). This motivates deriving a second temperature rescaling directly relevant for moist convection: the buoyancy of a non-entraining, moist static energy-conserving plume (Fig 4b, bottom, see SI B1b for its derivation):

$$\tilde{T}_{\text{buoyancy}}(p) \stackrel{\text{def}}{=} B_{\text{plume}}(q_{\text{NS}}, T, p), \quad [9]$$

where  $q_{\text{NS}} = q(p_{\text{NS}})$  is the near-surface specific humidity. This rescaling is inspired by recently introduced lower-tropospheric buoyancy measures (72, 73), but with an extension to the full troposphere (74). While Eq 9 does not explicitly include entrainment effects, the mapping of  $\tilde{T}_{\text{buoyancy}}(p)$  and  $\tilde{q}_{\text{RH}}(p)$  to heating and moisture sink will implicitly include these. This rescaling captures leading order effects needed to yield approximate climate invariance (Fig 4b) (Tab 1, rows 9 and 6). It also increases physical interpretability: Eq 9 links the vertical temperature structure and near-surface humidity changes to a metric that correlates well with deep convective activity (75). The presence of  $q_{\text{NS}}$  in Eq 9 captures the role of near-surface humidity relative to the temperature structure aloft in contributing to moist convective instability.

**Latent Heat Flux.** The last input whose distribution significantly changes with warming is the latent heat flux LHF (Fig 4c, top), and we refer the curious reader to SI B1c for the remaining inputs that change less with warming (sensible heat flux and surface pressure). Similarly to specific humidity, the increase of latent heat fluxes with warming is directly linked to the Clausius-Clapeyron relation (e.g., 76) (Tab 1, row 10), which motivates scaling LHF by near-surface specific humidity  $q(p_{\text{NS}})$  (Fig 4c, middle):

$$\tilde{\text{LHF}}_q \stackrel{\text{def}}{=} \frac{\text{LHF}}{L_v \max\{\epsilon_q, q(p_{\text{NS}})\}}, \quad [10]$$

where  $\epsilon_q$  is a user-chosen parameter that we can set to  $10^{-4}$  to avoid division by zero. While better than directly using LHF (Tab 1, row 11) this rescaling fails for very dry atmospheres when the latent heat flux is negative, e.g. in polar oceans where atmospheric water vapor may be condensing on the surface, or when the near-surface specific humidity is very small, e.g. in subtropical regions. To address this, we

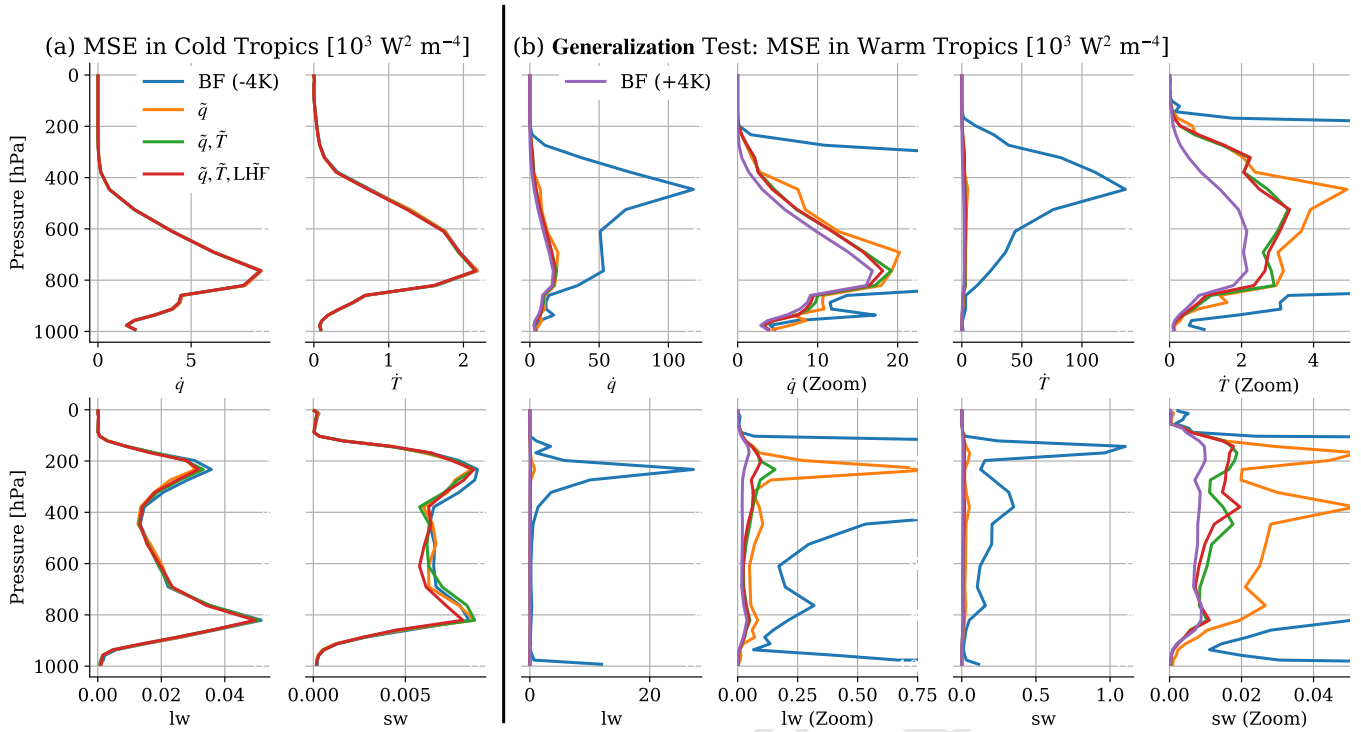


**Fig. 5.** Mean-squared error of subgrid thermodynamic tendencies versus pressure, horizontally-averaged over the Tropics of SPCAM3 aquaplanet simulations, for the four model outputs: total moistening ( $\tilde{q}$ ), total heating ( $\tilde{T}$ ), longwave heating (lw) and shortwave heating (sw). While the error is small for all NNs in the test set of the cold training climate (a), it is much larger in the test set of the warm test climate (b), but becomes progressively smaller as the inputs are successively rescaled: First no rescaling (blue), then specific humidity (orange), then temperature (green), then latent heat fluxes (red). For reference, the purple line depicts an NN trained in the warm climate. Given that the generalization error of the brute-force NN (blue line) greatly exceeds that of the rescaled NNs, we zoom in on each panel to facilitate visualization.

leverage the bulk aerodynamic formula to provide a physics-motivated rescaling of LHF using the near-surface saturation deficit (Fig 4c, bottom):

$$\tilde{\text{LHF}}_{\Delta q} \stackrel{\text{def}}{=} \frac{\text{LHF}}{L_v \max\{\epsilon_q, q_{\text{sat}}[T(p_{\text{NS}}), p_{\text{NS}}] - q(p_{\text{NS}})\}}. \quad [11]$$

Eq 11 rescales LHF, a thermodynamic variable, into  $\tilde{\text{LHF}}_{\Delta q}$ , approximately proportional to the magnitude of near-surface horizontal winds and density (e.g., 76), whose distributions vary less with warming. While both the Jensen-Shannon and Hellinger distances would suggest that  $\tilde{\text{LHF}}_{\Delta q}$  is a slightly less good rescaling than  $\tilde{\text{LHF}}_q$  (Tab 1, row 12) the  $\tilde{\text{LHF}}_{\Delta q}$  rescaling leads to improved generalization performance compared to  $\tilde{\text{LHF}}_q$  (not shown). This confirms that only considering the PDF distances is insufficient to find the optimal rescalings and underlines the importance of Fig 3’s workflow.

We now show that all three input rescalings ( $\tilde{q}_{\text{RH}}(\mathbf{p})$ ,  $\tilde{T}_{\text{buoyancy}}(\mathbf{p})$ , and  $\tilde{\text{LHF}}_{\Delta q}$ ) lead to statistically significant improvements in the ML models’ ability to generalize.

## Results

This section is organized as follows. After demonstrating the benefits of progressively rescaling the ML models’ inputs (Fig 5), we show how “climate-invariant” models learn subgrid closures across climates and geographies *during* training (Fig S5, Tab 2). We then discuss the global skill of different models *after* training (Fig 6, Fig S6, Fig 7) before finally investigating the structure of “climate-invariant” mappings to understand why they generalize better across climates of different temperatures (Fig 8).

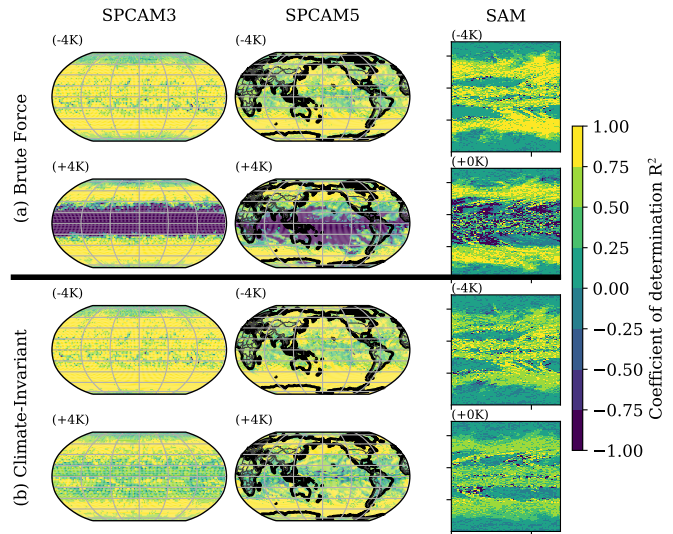


**Fig. 6.** Coefficient of determination  $R^2$  for 500hPa subgrid heating of brute-force (a) and climate-invariant (b) NNs trained using the cold (-4K) training set of each model (SPCAM3, SPCAM5, and SAM).  $R^2$  is calculated over the test sets of each cold (-4K) and warm (+4K) simulations.



Trained on	Model	Training Set	Validation Set	Training Set	Training Set
		Same temperature Same geography	Same temperature Same geography	Different temperature Same geography	Different geography
Cold Aquaplanet (-4K) SPCAM3	MLR BF	287 (288)	288 (289)	759 (785)	242 (265)
	MLR CI	294 (294)	295 (295)	671 (671)	245 (265)
	NN BF	172 (172)	172 (173)	2167 (2242)	1098 (1117)
	NN BF+DN	222 (222)	205 (206)	3225 (3509)	258 (318)
	NN CI+DN	168 (169)	169 (169)	422 (425)	297 (316)
Warm Aquaplanet (+4K) SPCAM3	MLR BF	642 (644)	643 (645)	328 (330)	507 (543)
	MLR CI	650 (651)	650 (651)	315 (315)	529 (598)
	NN BF	363 (364)	362 (364)	386 (472)	1354 (1612)
	NN BF+DN	473 (473)	434 (436)	248 (248)	728 (1275)
	NN CI	354 (355)	355 (356)	199 (202)	1241 (1293)
Cold Earth-like (-4K) SPCAM5	NN CI+DN	451 (451)	412 (414)	210 (212)	567 (659)
	MLR BF	197 (197)	197 (197)	508 (562)	299 (299)
	MLR CI	203 (203)	202 (202)	459 (459)	307 (307)
	NN BF	114 (114)	116 (116)	709 (803)	247 (251)
	NN BF+DN	165 (165)	152 (152)	512 (575)	247 (247)
SPCAM5	NN CI	112 (112)	114 (114)	292 (294)	312 (323)
NN CI+DN	158 (158)	144 (144)	346 (347)	229 (233)	

**Table 2. Mean-Squared Error (MSE, in units  $W^2 m^{-4}$ ) of six models trained in three simulations (first column) and evaluated over the training or validation set of the same and two other simulations (last four columns). The models (second column) are brute-force (BF) or climate-invariant (CI), multiple linear regressions (MLR) or neural nets (NN), and sometimes include dropout layers preceded by a batch normalization layer (DN). The models are trained for 20 epochs and we give the MSE corresponding to the epoch of minimal validation loss followed by the MSE averaged over the 5 epochs with lowest validation losses (in parentheses). In each application case, we highlight the best model’s error using bold font.**

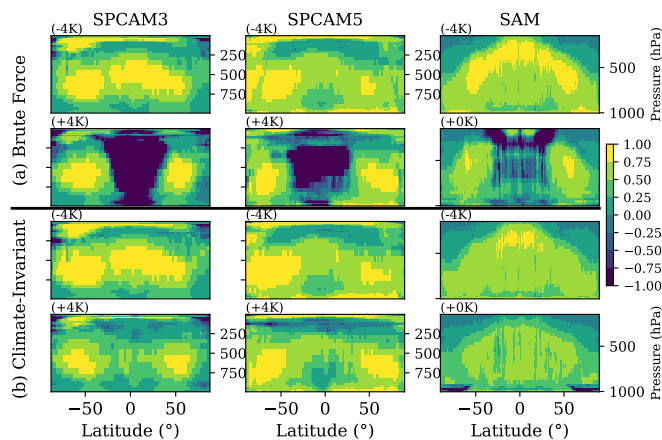


**Fig. 7.** Same as Fig 6, but averaging the samples used to calculate  $R^2$  for subgrid heating over (time,longitude) to obtain a (latitude,pressure) map.

**Benefits of Incremental Input Rescalings.** In this section, we demonstrate that incrementally rescaling the inputs of neural networks progressively improves their generalization abilities from the cold (-4K) aquaplanet (SPCAM3) simulation to the warm (+4K) aquaplanet simulation. The largest surface temperature jump tested in this study is between the cold aquaplanet simulation and the tropics of the warm aquaplanet simulation (“warm Tropics” for short), defined as the regions with out-of-distribution surface temperatures, whose latitudes are between  $-15^{\circ}S$  and  $23^{\circ}N$ . These regions approximately correspond to the red regions in the top-left subplots of Fig 2. Therefore, to expose the failure modes of the “brute force” model and the benefits of progressively rescaling the inputs, we first trained several NNs on the cold aquaplanet until they reached high accuracy (Fig 5a) before testing their generalization abilities out-of-distribution in the warm Tropics (Fig 5b).

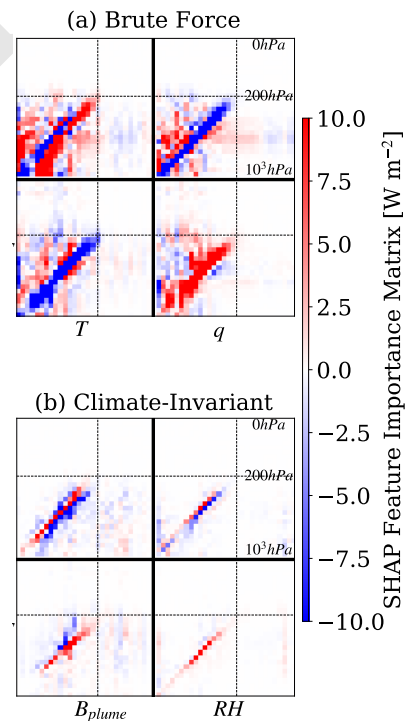


**Fig. 8.** SHAP feature importance matrix for the (a) brute-force and (b) climate-invariant neural nets trained in the cold (-4K) aquaplanet simulation (left), the warm (+4) warm aquaplanet simulation (middle), and their difference (right). To calculate these matrices, we sample inputs from the (+4K) warm aquaplanet simulation for all ML models to facilitate inter-model comparison. The x-axes indicate the vertical levels of the inputs, from the surface (left,  $10^3 hPa$ ) to the top of the atmosphere (right,  $0 hPa$ ), while the y-axes indicate the vertical levels of the outputs, from the surface (bottom,  $10^3 hPa$ ) to the top of the atmosphere (top,  $0 hPa$ ). We additionally indicate the 200hPa vertical level with dotted black lines.

In the cold Tropics, the vertical profiles of the mean-squared error (MSE) are nearly indiscernible for all types of NNs and roughly follow the vertical structure of subgrid variance, as discussed in (43, 45). When evaluated in the warm Tropics, the MSE of the “brute force” NN (blue line) increases by a factor of  $\approx 10$  and peaks above  $100\text{W}^2\text{m}^{-4}$ , underlining how *standard NNs fail to generalize across climates!* As discussed in the “Theory” Section, we progressively rescaled the inputs starting with the most important one: specific humidity, which is rescaled to relative humidity (orange line). This first rescaling decreases the MSE so much (by a factor of 5-10) that we need to zoom in on each panel to distinguish the generalization abilities of additional NNs. Adding the rescalings of temperature to plume buoyancy (green line) and then of LHF to  $\tilde{\text{LHF}}_{\Delta q}$  (red line) incrementally decrease the MSE, which is particularly clear for the subgrid longwave heating. Impressively, rescaling all three inputs decreases the MSE so much that *the resulting “climate-invariant” NN’s MSE (red line) is within  $\approx 25\%$  of the MSE of a “brute-force” NN that was directly trained in the warm climate (purple line).*

Hereafter, we use “climate-invariant” to refer to models for which all three inputs ( $q$ ,  $T$ , LHF) but no outputs (i.e., we do not assume knowledge of the output CDF across climate and geographies) were physically rescaled; after demonstrating their success in the aquaplanet case, we are now ready to investigate how these “climate-invariant” models learn in other climates and simulations introduced in the “Data” Section.

**Learning across Climates and Geographies.** In this section, we show that “climate-invariant” models learn mappings that are valid across climates and geographies, especially in conjunction with BN and DP layers.

Tab 2 shows the MSE of ML models trained in three different datasets, and evaluated over their training sets, validation sets, and over test sets of different temperature and geography. As discussed previously, “climate-invariant” NNs (NN CI) generalize better to warmer climates than “brute-force” NNs (NN BF). We can go one step further by examining learning curves, defined as the MSE of an ML model at the end of each epoch <sup>§</sup>. Impressively, the learning curve of the “climate-invariant” NN trained in the cold aquaplanet but tested in the warm aquaplanet (starred blue line in Fig S5a) is mostly decreasing, which is a key result of this manuscript: *“climate-invariant” NNs are able to continuously learn about subgrid thermodynamics in the warm aquaplanet as they are trained in the cold aquaplanet.* In contrast, the “brute-force” NN trained in the cold aquaplanet but tested in the warm aquaplanet makes extremely large generalization errors, which worsen as the model is trained in the cold aquaplanet (see SI D2 for details).

*“Climate-invariant” NNs also facilitate learning across geographies, i.e., from the aquaplanet to the Earth-like simulations and vice-versa (see NN CI rows in Tab 2).* “Climate-invariant” rescalings additionally improve the MLR baseline’s generalization ability, albeit less dramatically. This smaller improvement in MLR’s generalization abilities is linked to its relatively small number of free parameters, resulting in (1) “brute-force” MLRs generalizing better than “brute-force” NNs; and (2) MLRs having lower representation power and fitting their training sets less well, limiting the maximal accuracy of “climate-invariant” MLRs on test sets.

There are a few cases in which rescaling inputs does not fully solve the generalization problem, e.g., when trying to generalize from the aquaplanet to the Earth-like simulation. In that case, we leverage the fact that input rescalings can easily be combined with standard ML techniques to improve generalization, such as DP layers before each activation function and a single BN layer before the first DP layer (30). As DP layers randomly drop a fixed proportion of the free parameters during training, NNs with DP fit their training set less well (see NN CI+DN row of Tab 2). However, they improve generalization in difficult cases (e.g., between cold aquaplanet and Earth-like simulations) and do not overly deteriorate generalization in cases where the input rescalings work particularly well (e.g., from cold to warm aquaplanet). Our results suggest that *combining physics-guided generalization methods (e.g., physical rescaling of the inputs/outputs) with standard ML generalization methods (e.g., DP)* is advantageous and deserves further investigation. After analyzing the overall MSE during training, we now turn to the spatial characteristics of our ML models’ skill after training.

**Global Performance after Training.** In this section, we first compare the spatial characteristics of the “brute force” and “climate-invariant” NNs’ skill across climates of different temperatures to further establish the advantages of our “climate-invariant” rescaling. These advantages are clearly visible in Fig 6, where the “brute-force” models struggle to generalize to the warm Tropics for all simulations despite fitting the cold training set well (Fig 6a). We can trace these generalization errors to warm surface temperature conditions the NNs were not exposed to during training, visible when comparing Fig 6a with Fig 2a. In contrast, the “climate-invariant” models fit the warm climate almost as well as the cold climate they were trained in (Fig 6b)! Note that Fig 6 focuses on the horizontal map of a single output, i.e., the total subgrid heating at 500hPa, but that the horizontal map of other outputs, such as the near-surface subgrid heating (see Fig S5) all exhibit the same pattern of “brute-force” models failing in the warm Tropics and the “climate-invariant” models mostly correcting these generalization errors. Finally, the spatial distribution of the skill in the training set (e.g., middle column of Fig S6) is reassuringly consistent with the skill map of highly tuned NNs trained in similar conditions (e.g., 44). This confirms that our “brute-force” models are representative of state-of-the-art ML subgrid closures, and yet fail to generalize.

This failure is confirmed in the latitude-pressure map of the subgrid heating at all vertical levels shown in Fig 7a. In contrast, Fig 7b underlines how “climate-invariant” NNs improve generalization throughout the atmosphere in the warm Tropics without deteriorating skill in the mid-latitudes and poles of the warm simulation. This consideration helped us choose our final input rescaling, as the  $\tilde{T}_{\text{from NS}}$  temperature rescaling significantly deteriorated generalization in the mid-latitudes, while the  $\tilde{T}_{\text{buoyancy}}$  rescaling helps generalization in the Tropics without overly compromising skills at other latitudes. There is a slight skill compromise at high latitudes, as can be seen by comparing the second rows of Fig 7a and Fig 7b, which is especially apparent in the SAM case and can be partially traced back to challenges in generalizing subgrid ice sedimentation (not shown here, see 46, for details).

To fully compare ML models across climate and geographies, we list their overall MSEs in the training, validation, and both

<sup>§</sup>One epoch corresponds to the ML model being fed the entire training set once

generalization test sets in Table 2. In addition to the MSE of minimal validation loss, we show the MSE averaged over the 5 epochs of minimal validation loss in parentheses to confirm that our models have converged. Consistent with the learning curves shown in Fig S5, the generalization ability of “climate-invariant” NNs with DP and BN layers is best (two rightmost columns of each row’s NN CI+DN models). While they fit their training sets less well, “brute-force” MLRs generalize better than “brute-force” NNs because they have fewer free parameters (see MLR BF and NN BF models). In Tab 2, we also show that while DP and BN layers generally increase the generalization performance of “brute-force” NNs<sup>†</sup> (NN BF+DN models), we can systematically improve these standard ML generalization methods by combining them with input rescalings (NN CI+DN models).

Now that we have fully established the advantages of physical rescalings, we ask: Why do “climate-invariant” models generalize better than “brute force” ones?

**Understanding Climate Invariance.** In this section, we use a game theory-based explainable ML library, namely SHAP (77, 78), to dissect “climate-invariant” mappings and provide insight into why they generalize better across climates and geographies. Note that as MLRs are interpretable by construction, we can draw preliminary conclusions by visualizing MLR weights without the need for explainable ML libraries. Similarly, we can directly visualize the linear responses (71, 79–81) of NNs by calculating their Jacobians via automatic differentiation (e.g., 40). However, the difference between “brute-force” and “climate-invariant” MLRs is small and Jacobians cannot be reliably used to explain nonlinear NN predictions as they are first-order derivatives (82). Therefore, we present these two visualization methods in SI D4, and focus here on explaining the generalization abilities of NNs using SHAP, recalling that “climate-invariant” NNs are our best models at generalizing from cold to warm climates (see NN CI model in the first row and “Different temperature” column of Tab 2).

We select SHAP’s Kernel Explainer because of its versatility, as it can be used for any multi-inputs/outputs ML model, and specifically its “special weighted linear regression” option as our outputs are continuous making emulating subgrid closures a *regression* problem. For each output  $y_j$  of our ML model, SHAP estimates the effect of an input taking a particular value  $x_i$ ; SHAP is built based on a local accuracy property ensuring that the sum of each individual input’s effect equals how different  $y_j$  is from its average over the training set because of the whole input vector taking a particular value  $x$ :

$$\sum_{i=1}^{2N_p+4} \text{SHAP}(x_i, y_j) \stackrel{\text{def}}{=} y_j', \quad [12]$$

where we have introduced the deviation  $y_j'$ , defined as the difference between  $y_j$  and its training set average  $y_j' \stackrel{\text{def}}{=} y_j - \langle y_j \rangle_{\mathcal{E}}$ . We use these “Shapley values” to build a nonlinear feature matrix  $\mathcal{M}$  representing the effect of an input  $x_i$  on an output  $y_j$ :

$$\mathcal{M}_{ij} \stackrel{\text{def}}{=} \langle \text{sign}(x_i') \times \text{SHAP}(x_i, y_j) \rangle_{\mathcal{E}}, \quad [13]$$

<sup>†</sup>We have verified that in our case, DP and BN layers combined outperform DP layers only and BN layers only (not shown).

where we use the sign of the input deviation  $x_i'$  to make  $\mathcal{M}_{ij}$  positive if  $x_i'$  and  $y_j'$  have the same sign, e.g. if a positive input deviation leads to a positive output deviation<sup>‡</sup>.

In Fig 8, each rectangle depicts the SHAP feature matrix  $\mathcal{M}$  for a given model: “brute-force” (a) and “climate-invariant” (b), both trained in the warm aquaplanet simulation (second column). Focusing on a single feature matrix, the inputs of each model (e.g., specific humidity  $q$  and temperature  $T$ ) are organized on the x-axis from the surface ( $10^3$ hPa) to the top of the atmosphere (0hPa). The outputs of each model (subgrid moistening  $\dot{q}$  and subgrid heating  $\dot{T}$ ; see Fig S11 for subgrid longwave heating lw and subgrid shortwave heating sw) are organized on the y-axis, from the surface to the top of the atmosphere. We use dotted lines to depict the 200hPa isobars. Following a horizontal line shows how different inputs contribute to a given output, while following a vertical line shows how a given input influences different outputs.

Fig 8 contains a wealth of information about subgrid closures trained in aquaplanet simulations; we focus here on visualizing how the “climate-invariant” NNs (b) operate in ways that generalize better than their “brute-force” counterpart (a). Consider the row for subgrid heating  $\dot{T}$ . In the “brute-force” case (a),  $\mathcal{M}$  has large coefficients in the entire troposphere (in the entire square below the dashed lines depicting the approximate tropopause level). This means that specific humidity and temperature deviations at all levels impact subgrid heating at a given level, i.e. there are large non-local relations in the vertical. Some non-local relations are physically plausible for convection, since buoyant plumes tend to rise from the surface, and indeed near-surface  $T$  and  $q$  influence  $\dot{T}$  through the entire troposphere. However, moisture at higher altitudes influences  $\dot{T}$  at lower altitudes, raising suspicions that some aspects of this non-locality are not causal, as (40) show can happen in brute force NNs. Temperature variations are observed to have strong vertical correlations (83) in part because of deep convective effects. Because temperature affects the saturation threshold for moisture, the NN will have to correctly capture the effects of both temperature and moisture wherever either has influence. In contrast, in the  $B_{plume}$ -RH “climate-invariant” case (b), leading nonlocal effects between the boundary layer and the free troposphere have already been taken into account in the buoyancy formulation, and the temperature-dependent saturation threshold is built into RH. Thus,  $\mathcal{M}$  for  $\dot{T}$  tends to be concentrated near the red diagonal, meaning that positive deviations of plume buoyancy and relative humidity increase subgrid heating near the same vertical level. The use of domain knowledge has effectively reduced the effects that must be estimated by the NN for the “climate-invariant” models. This tends to yield differences between the models trained in the cold and the warm climates that are much smaller than for the “brute-force” models (see last column of Fig S11).

## Conclusion

In the context of climate change, we hypothesized that ML models emulating “climate-invariant” mappings (Fig 1, Fig 3), for which the distributions of inputs/outputs change little

<sup>‡</sup>In the particular case of the MLR defined in Eq 18 of the SI, the nonlinear feature matrix becomes the regression weight matrix multiplied by the absolute value of the input deviations:  $\mathcal{M}_{ij} = \langle A_{ij} |x_i'| \rangle_{\mathcal{E}}$ , confirming that the feature matrix  $\mathcal{M}$  is a nonlinear extension of the Jacobian ( $A$  in the MLR case).



across climates (Fig 4), generalize much better than ML models emulating “brute-force” mappings, for which the distributions of inputs/outputs change significantly across climates. Tested on a suite of storm-resolving simulations with different surface temperatures in three distinct climate models with different geographies (Fig 2), physically-rescaled NNs generalize better to a warmer climate as their inputs are progressively rescaled (Fig 5). “Climate-invariant” NNs whose inputs have all been rescaled learn mappings that hold across temperatures and geographies during training (Tab 2), and hence exhibit superior generalization skill almost everywhere on the globe (Fig 6, Fig 7). Finally, attribution maps reveal that “climate-invariant” NNs learn more spatially local mappings that facilitate generalization across climates (Fig 8).

From a computational perspective, incorporating physical knowledge of climate change into an ML framework to improve its generalization skill is a successful example of using domain knowledge to extract more informative predictors, informally referred to as “feature engineering” (e.g., 84). This also aids interpretability of the mapping. From a climate science perspective, requiring that a nonlinear statistical model of the atmosphere generalize across climate is a stringent test that helped us discover a new mapping. As this “climate-invariant” mapping is more robust to climate and geography changes, it appears to be more advantageous than directly using model and observational outputs (e.g., specific humidity, temperature), even when data are available in various climate regimes. In the particular case of subgrid thermodynamics, our generalization results suggest the possibility of NN-powered closures that could work in Earth-like settings, even in vastly different climate conditions. The attribution maps suggest the possibility of new analytic representations of convection from data, facilitated by the more local “climate-invariant” representation of subgrid thermodynamics.

**ACKNOWLEDGMENTS.** TB and MP acknowledge funding from NSF grants OAC1835863 and AGS-1734164. MP acknowledges partial funding from the DOE “Enabling Aerosol-cloud interactions at Global convection-permitting scales (EAGLES)” project (74358), funded by the U.S. Department of Energy, Office of Science, Office of Biological and Environmental Research, Earth System Model Development (ESMD) program. JY acknowledges support from the EAPS Houghton-Lorenz postdoctoral fellowship. PG thanks NSF grant AGS-1734164 as well as USMILE European Research Council grant. PG, POG, and JY acknowledge funding from M<sup>2</sup>LInES Schmidt Future funding. FA and JDN acknowledge NSF AGS-1936810. We also thank the Extreme Science and Engineering Discovery Environment supported by NSF grant number ACI-1548562 (charge numbers TG-ATM190002 and TG-ATM170029), and HPC support from Cheyenne (doi:10.5065/D6RX99HX) provided by NCAR’s Computational and Information Systems Laboratory (sponsored by the NSF) for computational resources. We thank William Boos for providing the SAM hypohydrostatic simulation output, Andrea Jenney, Imme Ebert-Uphoff, and the CBRAIN discussion group for help and advice that greatly benefited the present manuscript.

1. M Reichstein, et al., Deep learning and process understanding for data-driven earth system science. *Nature* **566**, 195–204 (2019).
2. T Beucler, I Ebert-Uphoff, S Rasp, M Pritchard, P Gentine, Machine learning for clouds and climate in *Clouds and Climate*. (AGU Geophysical Monograph Series), (2021).
3. C Irrgang, et al., Towards neural earth system modelling by integrating artificial intelligence in earth system science. *Nat. Mach. Intell.* **3**, 667–674 (2021).
4. P Ukkonen, R Pincus, RJ Hogan, K Pagh Nielsen, E Kaas, Accelerating radiation computations for dynamical models with targeted machine learning and code optimization. *J. Adv. Model. Earth Syst.* **12**, e2020MS002226 (2020).
5. A Belochitski, et al., Tree approximation of the long wave radiation parameterization in the ncar cam global climate model. *J. Comput. Appl. Math.* **236**, 447–460 (2011).
6. JJ Gristey, G Feingold, IB Glenn, KS Schmidt, H Chen, On the relationship between shal-

- low cumulus cloud field properties and surface solar irradiance. *Geophys. Res. Lett.* **47**, e2020GL090152 (2020).
7. R Lagerquist, D Turner, I Ebert-Uphoff, J Stewart, V Hagerty, Using deep learning to emulate and accelerate a radiative transfer model. *J. Atmospheric Ocean. Technol.* **38**, 1673–1696 (2021).
8. M Chantry, S Hatfield, P Dueben, I Polichtchouk, T Palmer, Machine learning emulation of gravity wave drag in numerical weather forecasting. *J. Adv. Model. Earth Syst.* **13**, e2021MS002477 (2021).
9. Z Espinosa, A Sheshadri, G Cain, E Gerber, K DallaSanta, Machine learning emulation of parameterized gravity wave momentum fluxes in an atmospheric global climate model in *EGU General Assembly Conference Abstracts*. pp. EGU21–1398 (2021).
10. D Matsuoka, et al., Application of deep learning to estimate atmospheric gravity wave parameters in reanalysis data sets. *Geophys. Res. Lett.* **47**, e2020GL089436 (2020).
11. H Morrison, M van Lier-Walqui, MR Kumjian, OP Prat, A bayesian approach for statistical-physical bulk parameterization of rain microphysics. part i: Scheme description. *J. Atmospheric Sci.* **77**, 1019–1041 (2020).
12. A Seifert, S Rasp, Potential and limitations of machine learning for modeling warm-rain cloud microphysical processes. *J. Adv. Model. Earth Syst.* **12**, e2020MS002301 (2020).
13. A Gettelman, et al., Machine learning the warm rain process. *J. Adv. Model. Earth Syst.* **13**, e2020MS002268 (2021).
14. B Francois, S Thao, M Vrac, Adjusting spatial dependence of climate model outputs with cycle-consistent adversarial networks. *Clim. Dyn.* **57**, 3323–3353 (2021).
15. B Pan, et al., Learning to correct climate projection biases. *J. Adv. Model. Earth Syst.* **13**, e2021MS002509 (2021).
16. V Zantedeschi, et al., Cumulo: A dataset for learning cloud classes. *arXiv preprint arXiv:1911.04227* (2019).
17. S Rasp, H Schultz, S Bony, B Stevens, Combining crowdsourcing and deep learning to explore the mesoscale organization of shallow convection. *Bull. Am. Meteorol. Soc.* **101**, E1980–E1995 (2020).
18. D Watson-Parris, S Sutherland, M Christensen, R Eastman, P Stier, A large-scale analysis of pockets of open cells and their radiative impact. *Geophys. Res. Lett.* **48**, e2020GL092213 (2021).
19. L Denby, Discovering the importance of mesoscale cloud organization through unsupervised classification. *Geophys. Res. Lett.* **47**, e2019GL085190 (2020).
20. Y Han, GJ Zhang, X Huang, Y Wang, A moist physics parameterization based on deep learning. *J. Adv. Model. Earth Syst.* **12**, e2020MS002076 (2020).
21. ND Brenowitz, CS Bretherton, Prognostic validation of a neural network unified physics parameterization. *Geophys. Res. Lett.* **45**, 6289–6298 (2018).
22. VM Krasnopolsky, MS Fox-Rabinovitz, AA Belochitski, Using ensemble of neural networks to learn stochastic convection parameterizations for climate and numerical weather prediction models from data simulated by a cloud resolving model. *Adv. Artif. Neural Syst.* **2013** (2013).
23. L Breiman, Random forests. *Mach. learning* **45**, 5–32 (2001).
24. PA O’Gorman, JG Dwyer, Using machine learning to parameterize moist convection: Potential for modeling of climate, climate change, and extreme events. *J. Adv. Model. Earth Syst.* **10**, 2548–2563 (2018).
25. S Rasp, MS Pritchard, P Gentine, Deep learning to represent subgrid processes in climate models. *Proc. Natl. Acad. Sci.* **115**, 9684–9689 (2018).
26. T Beucler, M Pritchard, P Gentine, S Rasp, Towards physically-consistent, data-driven models of convection in *IGARSS 2020-2020 IEEE International Geoscience and Remote Sensing Symposium*. (IEEE), pp. 3987–3990 (2020).
27. MJ Molina, DJ Gagne, AF Prein, A benchmark to test generalization capabilities of deep learning methods to classify severe convective storms in a changing climate. *Earth Space Sci. Open Arch. ESSOAr* (2021).
28. Y LeCun, Y Bengio, et al., Convolutional networks for images, speech, and time series. *The handbook brain theory neural networks* **3361**, 1995 (1995).
29. C Liu, et al., Continental-scale convection-permitting modeling of the current and future climate of north america. *Clim. Dyn.* **49**, 71–95 (2017).
30. S Ioffe, C Szegedy, Batch normalization: Accelerating deep network training by reducing internal covariate shift in *International conference on machine learning*. (PMLR), pp. 448–456 (2015).
31. N Srivastava, G Hinton, A Krizhevsky, I Sutskever, R Salakhutdinov, Dropout: a simple way to prevent neural networks from overfitting. *The journal machine learning research* **15**, 1929–1958 (2014).
32. X Ying, An overview of overfitting and its solutions in *Journal of Physics: Conference Series*. (IOP Publishing), Vol. 1168, p. 022022 (2019).
33. SJ Pan, Q Yang, A survey on transfer learning. *IEEE Transactions on knowledge data engineering* **22**, 1345–1359 (2009).
34. VM Patel, R Gopalan, R Li, R Chellappa, Visual domain adaptation: A survey of recent advances. *IEEE signal processing magazine* **32**, 53–69 (2015).
35. D Tuia, C Persello, L Bruzzone, Domain adaptation for the classification of remote sensing data: An overview of recent advances. *IEEE geoscience remote sensing magazine* **4**, 41–57 (2016).
36. D Randall, M Khairoutdinov, A Arakawa, W Grabowski, Breaking the Cloud Parameterization Deadlock. *Bull. Am. Meteorol. Soc.* **84**, 1547–1564 (2003).
37. S Bony, et al., Clouds, circulation and climate sensitivity. *Nat. Geosci.* **8**, 261–268 (2015).
38. T Schneider, et al., Climate goals and computing the future of clouds. *Nat. Clim. Chang.* **7**, 3–5 (2017).
39. P Gentine, V Eyring, T Beucler, Deep learning for the parametrization of subgrid processes in climate models. *Deep. Learn. for Earth Sci. A Compr. Approach to Remote. Sensing, Clim. Sci. Geosci.* pp. 307–314 (2021).
40. ND Brenowitz, T Beucler, M Pritchard, CS Bretherton, Interpreting and stabilizing machine-learning parametrizations of convection. *J. Atmospheric Sci.* **77**, 4357–4375 (2020).
41. J Ott, et al., A fortran-keras deep learning bridge for scientific computing. *Sci. Program.* **2020** (2020).

42. P Forster, et al., The earth's energy budget, climate feedbacks, and climate sensitivity. *Clim. Chang.* (2021).
43. T Beucler, et al., Enforcing analytic constraints in neural networks emulating physical systems. *Phys. Rev. Lett.* **126**, 098302 (2021).
44. G Mooers, et al., Assessing the potential of deep learning for emulating cloud superparameterization in climate models with real-geography boundary conditions. *J. Adv. Model. Earth Syst.* **13**, e2020MS002385 (2021).
45. P Gentine, M Pritchard, S Rasp, G Reinaudi, G Yacalis, Could machine learning break the convection parameterization deadlock? *Geophys. Res. Lett.* **45**, 5742–5751 (2018).
46. J Yuval, PA O'Gorman, Stable machine-learning parameterization of subgrid processes for climate modeling at a range of resolutions. *Nat. communications* **11**, 1–10 (2020).
47. M Khairoutdinov, D Randall, C DeMott, Simulations of the atmospheric general circulation using a cloud-resolving model as a superparameterization of physical processes. *J. Atmospheric Sci.* **62**, 2136–2154 (2005).
48. MS Pritchard, CS Bretherton, Causal evidence that rotational moisture advection is critical to the superparameterized madden–julian oscillation. *J. Atmospheric Sci.* **71**, 800–815 (2014).
49. JA Andersen, Z Kuang, Moist static energy budget of mjo-like disturbances in the atmosphere of a zonally symmetric aquaplanet. *J. Clim.* **25**, 2782–2804 (2012).
50. MF Khairoutdinov, DA Randall, A cloud resolving model as a cloud parameterization in the ncar community climate system model: Preliminary results. *Geophys. Res. Lett.* **28**, 3617–3620 (2001).
51. M Wang, et al., A multiscale modeling framework model (superparameterized cam5) with a higher-order turbulence closure: Model description and low-cloud simulations. *J. Adv. Model. Earth Syst.* **7**, 484–509 (2015).
52. JW Hurrell, JJ Hack, D Shea, JM Caron, J Rosinski, A new sea surface temperature and sea ice boundary dataset for the community atmosphere model. *J. Clim.* **21**, 5145–5153 (2008).
53. SN Tulich, A strategy for representing the effects of convective momentum transport in multi-scale models: Evaluation using a new superparameterized version of the weather research and forecast model (SP-WRF). *J. Adv. Model. Earth Syst.* **7**, 938–962 (2015).
54. ND Brenowitz, CS Bretherton, Spatially extended tests of a neural network parameterization trained by coarse-graining. *J. Adv. Model. Earth Syst.* **11**, 2728–2744 (2019).
55. T Bolton, L Zanna, Applications of deep learning to ocean data inference and subgrid parameterization. *J. Adv. Model. Earth Syst.* **11**, 376–399 (2019).
56. ST Garner, D Frierson, I Held, O Pauluis, G Vallis, Resolving convection in a global hypohydrostatic model. *J. atmospheric sciences* **64**, 2061–2075 (2007).
57. WR Boos, A Fedorov, L Muir, Convective self-aggregation and tropical cyclogenesis under the hypohydrostatic rescaling. *J. Atmospheric Sci.* **73**, 525–544 (2016).
58. P O'Gorman, Z Li, W Boos, J Yuval, Response of extreme precipitation to uniform surface warming in quasi-global aquaplanet simulations at high resolution. *Philos. Transactions Royal Soc. A* **379**, 20190543 (2021).
59. RB Neale, BJ Hoskins, A standard test for agcms including their physical parametrizations: I: The proposal. *Atmospheric Sci. Lett.* **1**, 101–107 (2000).
60. A Karpatne, I Ebert-Uphoff, S Ravela, HA Bubaie, V Kumar, Machine learning for the geosciences: Challenges and opportunities. *IEEE Transactions on Knowl. Data Eng.* **31**, 1544–1554 (2018).
61. TG Shepherd, Symmetries, conservation laws, and hamiltonian structure in geophysical fluid dynamics in *Advances in Geophysics*. (Elsevier) Vol. 32, pp. 287–338 (1990).
62. R Beran, Minimum hellinger distance estimates for parametric models. *The annals Stat.* pp. 445–463 (1977).
63. DM Endres, JE Schindelin, A new metric for probability distributions. *IEEE Transactions on Inf. theory* **49**, 1858–1860 (2003).
64. JR Holton, An introduction to dynamic meteorology. *Am. J. Phys.* **41**, 752–754 (1973).
65. AP Siebesma, S Bony, C Jakob, B Stevens, *Clouds and Climate: Climate Science's Greatest Challenge*. (Cambridge University Press), (2020).
66. RG Brown, C Zhang, Variability of midtropospheric moisture and its effect on cloud-top height distribution during TOGA COARE. *J. atmospheric sciences* **54**, 2760–2774 (1997).
67. CS Bretherton, ME Peters, LE Back, Relationships between water vapor path and precipitation over the tropical oceans. *J. Clim.* **17**, 1517–1528 (2004).
68. CE Holloway, JD Neelin, Moisture vertical structure, column water vapor, and tropical deep convection. *J. Atmos. Sci.* **66**, 1665–1683 (2009).
69. JT Seeley, N Jeevanjee, DM Roms, Fat or fit: Are anvil clouds or the tropopause temperature invariant? *Geophys. Res. Lett.* **46**, 1842–1850 (2019).
70. DL Hartmann, K Larson, An important constraint on tropical cloud-climate feedback. *Geophys. research letters* **29**, 12–1 (2002).
71. Z Kuang, DL Hartmann, Testing the fixed anvil temperature hypothesis in a cloud-resolving model. *J. Clim.* **20**, 2051–2057 (2007).
72. F Ahmed, JD Neelin, Reverse engineering the tropical precipitation–buoyancy relationship. *J. Atmospheric Sci.* **75**, 1587–1608 (2018).
73. F Ahmed, ÁF Adames, JD Neelin, Deep convective adjustment of temperature and moisture. *J. Atmospheric Sci.* **77**, 2163–2186 (2020).
74. KA Schiro, F Ahmed, SE Giangrande, JD Neelin, GoAmazon2014/5 campaign points to deep-inflow approach to deep convection across scales. *Proc. Natl. Acad. Sci.* **115**, 201719842 (2018).
75. F Ahmed, JD Neelin, Protected convection as a metric of dry air influence on precipitation. *J. Clim.* **34**, 3821–3838 (2021).
76. DL Hartmann, *Global physical climatology*. (Newnes) Vol. 103, (2015).
77. SM Lundberg, SI Lee, A unified approach to interpreting model predictions in *Proceedings of the 31st international conference on neural information processing systems*. pp. 4768–4777 (2017).
78. LS Shapley, *17. A value for n-person games*. (Princeton University Press), (2016).
79. MJ Herman, Z Kuang, Linear response functions of two convective parameterization schemes. *J. Adv. Model. Earth Syst.* **5**, 510–541 (2013).
80. T Beucler, T Cronin, K Emanuel, A linear response framework for radiative-convective instability. *J. Adv. Model. Earth Syst.* **10**, 1924–1951 (2018).
81. Z Kuang, Linear stability of moist convecting atmospheres. part i: From linear response functions to a simple model and applications to convectively coupled waves. *J. Atmospheric Sci.* **75**, 2889–2907 (2018).
82. PJ Kindermans, et al., The (un) reliability of saliency methods in *Explainable AI: Interpreting, Explaining and Visualizing Deep Learning*. (Springer), pp. 267–280 (2019).
83. CE Holloway, JD Neelin, The convective cold top and quasi equilibrium. *J. atmospheric sciences* **64**, 1467–1487 (2007).
84. A Zheng, A Casari, *Feature engineering for machine learning: principles and techniques for data scientists*. (" O'Reilly Media, Inc."), (2018).

## Supplementary Information for

### Climate-Invariant Machine Learning

TB, MP, JY, AG, LP, SR, FA, POG, JDN, NL, PG

Tom Beucler.

E-mail: [tom.beucler@gmail.com](mailto:tom.beucler@gmail.com)

#### This PDF file includes:

- Supplementary text
- Figs. S1 to S12
- Tables S1 to S2
- SI References

#### Supporting Information Text

The Supplementary Information (SI) is organized as follows: First, we discuss code and data availability (SI A), including links to multiple repositories to reproduce the different ML-based closures and climate simulations discussed in the manuscript. Then, we derive the input rescalings used in the manuscript (SI B1), the output rescalings tested in this SI (SI B2), and discuss possible vertical coordinate rescalings (SI B3). SI C details the practical implementation of our “climate-invariant” ML workflow. Finally, we present supplementary results in SI D, including the Jensen-Shannon distance between input distributions to complement the Hellinger distance presented in the main manuscript (SI D1), the learning curves of “climate-invariant” models across climates and geographies (SI D2), the generalization skill of “climate-invariant” NNs near the surface (SI D3), and three methods to visualize the “brute-force” and “climate-invariant” mappings and compare them in the cold (-4K) and warm (+4K) climates.

#### A. Code and Data Availability

The code used to process data, train models, and produce this manuscript’s figure can be found in the following Github repository: <https://github.com/tbeucler/CBRAIN-CAM>, which is archived using Zenodo <https://zenodo.org/record/5775489#>.

This repository includes a notebook to reproduce all the figures in this manuscript [https://github.com/tbeucler/CBRAIN-CAM/blob/master/notebooks/tbeucler\\_devlog/077\\_Climate\\_Invariant\\_Paper\\_Figures.ipynb](https://github.com/tbeucler/CBRAIN-CAM/blob/master/notebooks/tbeucler_devlog/077_Climate_Invariant_Paper_Figures.ipynb), as well as a brief guide on how to train a “climate-invariant” neural network and verify its improved generalization ability: [https://github.com/tbeucler/CBRAIN-CAM/blob/master/Climate\\_Invariant\\_Guide.ipynb](https://github.com/tbeucler/CBRAIN-CAM/blob/master/Climate_Invariant_Guide.ipynb). Both scripts rely on the manuscript’s accompanying data, archived in the following Zenodo repository: <https://zenodo.org/record/1402384#>.

The above Github repository is forked from (and builds upon) Stephan Rasp’s CBRAIN repository <https://github.com/raspstephan/CBRAIN-CAM>, also archived using Zenodo <https://zenodo.org/record/1402384#>. This repository contains a quickstart guide <https://github.com/raspstephan/CBRAIN-CAM/blob/master/quickstart.ipynb> to preprocess raw climate model output, train a neural network and benchmark it.

As described in the “Data” section, we use data from eight climate simulations using three climate models (SPCAM3, SPCAM5, and SAM) to form our training, validation, and test sets. We report the exact characteristics of the splits in Tab S1 and information to re-generate the full simulation



output below.

**SPCAM3** The codebase for running the ‘‘SPCAM3’’ simulation is the same employed by (4), which is archived at <https://gitlab.com/mspritch/spcam3.0-neural-net/-/tree/sp-diagnostic> for the (+0K) simulation. The sea surface temperature is uniformly cooled by 4K to produce the (-4K) simulation and uniformly warmed by 4K to produce the (+4K) simulation. Raw output of the (+0K) simulation can be found at <https://zenodo.org/record/1402384#.YaUCsdDMI-w> (3). The full simulations output, which is several TB, is archived on the GreenPlanet cluster at UC Irvine and available upon request.

**SPCAM5** The codebase for running the ‘‘SPCAM5’’ simulations is the same employed by (5), which is archived at [https://github.com/mspritch/UltraCAM-spcam2\\_0\\_cesm1\\_1\\_1](https://github.com/mspritch/UltraCAM-spcam2_0_cesm1_1_1); this code was in turn forked from a development version of the CESM1.1.1 located on the NCAR central subversion repository under tag `spcam_cam5_2_00_forCESM1_1_1Rel_V09`, which dates to February 25, 2013. The full simulations output, which is several TB, is also archived on the GreenPlanet cluster at UC Irvine and available upon request. We additionally archived the input data and run scripts necessary to re-run all three simulations as part of the manuscript’s accompanying data using Zenodo <https://zenodo.org/record/5775541#.YbeMHNDMKUI> (2).

**SAM** The codebase for running the ‘‘SAM’’ simulations is the same employed by (6). The data from the (-4K) simulation is several TB and can be found at [https://drive.google.com/drive/folders/1TRPDL6JkclJgTHJL9lb\\_Z4XuPyvNVlyY](https://drive.google.com/drive/folders/1TRPDL6JkclJgTHJL9lb_Z4XuPyvNVlyY). The initial sounding, meridional surface temperature profile, and source code to re-run the simulation can be found at [https://zenodo.org/record/4118346#.YaT\\_WtBKg-w](https://zenodo.org/record/4118346#.YaT_WtBKg-w) (7). To produce the (+0K) simulation, the initial sounding and surface temperature profiles are both uniformly warmed by 4K.

## B. Physical Rescalings

### B1. Inputs.

**B1a. Relative Humidity.** Relative humidity is defined as the ratio of the partial pressure of water vapor  $e(\mathbf{p}, \mathbf{q})$  to its saturation value  $e_{\text{sat}}(T)$ , and can be expressed analytically:

$$\text{RH} \stackrel{\text{def}}{=} \frac{e(\mathbf{p}, \mathbf{q})}{e_{\text{sat}}(T)} \stackrel{q \ll 1}{\approx} \frac{R_v}{R_d} \frac{p\mathbf{q}}{e_{\text{sat}}(T)}, \quad [1]$$

where  $R_v \approx 461 \text{ J kg}^{-1} \text{ K}^{-1}$  is the specific gas constant for water vapor,  $R_d \approx 287 \text{ J kg}^{-1} \text{ K}^{-1}$  is the specific gas constant for dry air,  $p$  (in units Pa) is the total atmospheric pressure,  $\mathbf{q}$  (in units kg/kg) is specific humidity, and  $e_{\text{sat}}(T)$  (in units Pa) is the saturation pressure of water vapor, whose analytic expression in our case is given below. Consistent with Eq 1, the saturation specific humidity  $\mathbf{q}_{\text{sat}}$  corresponding to  $\text{RH} = 1$ , is

$$\mathbf{q}_{\text{sat}}(T, p) = \frac{R_d e_{\text{sat}}(T)}{R_v p}. \quad [2]$$

SAM’s single-moment microphysics scheme (8) partitions water between the liquid and ice phases using a weight  $\omega$  that is a linear function of the absolute temperature:

$$\omega \stackrel{\text{def}}{=} \frac{T - T_{00}}{T_0 - T_{00}}. \quad [3]$$

Under the assumptions of this microphysics scheme, the saturation pressure of water vapor can then be found by integrating the Clausius-Clapeyron equation with respect to temperature, expressed analytically as:

$$e_{\text{sat}}(T) = \begin{cases} e_{\text{liq}}(T) & T > T_0 \\ e_{\text{ice}}(T) & T < T_{00} \\ \omega e_{\text{liq}}(T) + (1 - \omega) e_{\text{ice}}(T) & T \in [T_{00}, T_0] \end{cases}, \quad [4]$$

where  $T_0 = 273.16 \text{ K}$  and  $T_{00} = 253.16 \text{ K}$ . In Eq 4, as temperature increases, the saturation pressure of water vapor goes from the saturation vapor pressure with respect to liquid  $e_{\text{liq}}$ , to the saturation vapor pressure with respect to ice  $e_{\text{ice}}$ . These are given by the following polynomial approximations:

$$e_{\text{liq}}(T) = 100 \text{ Pa} \times \sum_{i=0}^8 a_{\text{liq},i} [\max(-193.15 \text{ K}, T - T_0)]^i, \quad [5]$$

where  $\mathbf{a}_{\text{liq}}$  is a vector of length 9 containing nonzero polynomial coefficients. The polynomial approximation for  $e_{\text{ice}}$ , with the same temperature switches as Eq 4, is:

$$e_{\text{ice}}(T) = \begin{cases} e_{\text{liq}}(T) \\ 100 \text{ Pa} \times \{c_{\text{ice},1} + \mathcal{C}(T) [c_{\text{ice},4} + c_{\text{ice},5} \mathcal{C}(T)]\} \\ 100 \text{ Pa} \times \sum_{i=0}^8 a_{\text{ice},i} (T - T_0)^i \end{cases}, \quad [6]$$

where  $\mathcal{C}(T)$  is a ramp function of temperature given by:

$$\mathcal{C}(T) \stackrel{\text{def}}{=} \max(c_{\text{ice},2}, T - T_0), \quad [7]$$

and  $(\mathbf{a}_{\text{ice}}, \mathbf{c}_{\text{ice}})$  are vectors of length 9 and 5 containing nonzero elements, respectively. Between temperatures of  $T_{00}$  and  $T_0$ , the saturation pressure of water vapor is a weighted mean of  $e_{\text{liq}}$  and  $e_{\text{ice}}$ . The reader interested in the numerical details of this rescaling is referred to our implementation of relative humidity at [code link].

**B1b. Plume Buoyancy.** Buoyancy is defined as the upward acceleration exerted upon parcels by virtue of the density difference between the parcel and the surrounding air of the atmospheric column (e.g., 9). Because our ML model’s inputs represent the large-scale thermodynamic state, the ML model does not have information about the storm-scale buoyancy field, and we must rely on idealized approximations to estimate the buoyancy that a plume would have for given specific humidity and temperature profiles. To be consistent with the model’s conserved quantities (8), we derive a simple buoyancy metric based on a moist static energy ( $h$ ) conserving plume below following similar derivations in (10) and (11). We refer the reader interested in the numerical details of this rescaling to [code link].

For purposes of this rescaling, we omit virtual temperature effects and condensate loading (effects of the environmental water vapor on heating/moisture sink are being estimated separately). Thus the parcel buoyancy is simply proportional to the relative difference between its temperature  $T_{\text{par}}$  and the environmental temperature  $T$ :

$$\mathbf{B}_{\text{plume}} \approx g \frac{T_{\text{par}} - T}{T}, \quad [8]$$

where  $g$  is the gravity constant. Further assuming that the plume is non-entraining, obeys hydrostatic balance, and lifts

parcels from the near-surface, the lifted parcel's moist static energy is conserved and equal to its near-surface value (at pressure  $p_{\text{NS}}$ ):

$$h_{\text{par}} \approx h(p_{\text{NS}}) \stackrel{\text{def}}{=} L_v q(p_{\text{NS}}) + c_p T(p_{\text{NS}}), \quad [9]$$

where we have used the environmental moist static energy's definition:

$$\mathbf{h} \stackrel{\text{def}}{=} L_v \mathbf{q} + c_p \mathbf{T} + g\mathbf{z}, \quad [10]$$

where  $\mathbf{z}$  is geopotential height, and we neglected  $z(p_{\text{NS}})$  as the near-surface is close to the surface by definition. To express the parcel's buoyancy as a function of the environmental thermodynamic state, we finally assume that the parcel is saturated\*, and that the thermodynamic differences between the parcel and the environment are small, which allows us to linearize the Clausius-Clapeyron equation about the environmental temperature:

$$\begin{aligned} T_{\text{par}} - \mathbf{T} &\stackrel{\text{Claus.}-\text{Clap.}}{\approx} \left( \frac{\partial T}{\partial q^*} \right)_{\mathbf{T}, \mathbf{p}} (q_{\text{sat, par}} - q_{\text{sat}}) \\ &= \frac{R_v \mathbf{T}^2}{L_v q_{\text{sat}}} (q_{\text{sat, par}} - q_{\text{sat}}) \\ &= \frac{R_v \mathbf{T}^2}{L_v^2 q_{\text{sat}}} [h_{\text{par}} - \mathbf{h}_{\text{sat}} - c_p (T_{\text{par}} - \mathbf{T})]. \end{aligned} \quad [11]$$

Using Eq 11 to write  $T_{\text{par}} - \mathbf{T}$  as a function of the environmental thermodynamic state and substituting the resulting expression into Eq 8 yields an estimation of plume buoyancy from  $(\mathbf{q}, \mathbf{T}, \mathbf{p})$ :

$$\mathbf{B}_{\text{plume}}(\mathbf{q}, \mathbf{T}, \mathbf{p}) = \frac{g [h_{\text{par}} - \mathbf{h}_{\text{sat}}(\mathbf{q}, \mathbf{T}, \mathbf{p})]}{\kappa(\mathbf{T}, \mathbf{p}) \times c_p \mathbf{T}}, \quad [12]$$

where the parcel's moist static energy is expressed as a function of near-surface  $(q, T)$  in Eq 9, the environmental saturated moist static energy in pressure coordinates is defined as:

$$\mathbf{h}_{\text{sat}}(\mathbf{q}, \mathbf{T}, \mathbf{p}) \stackrel{\text{def}}{=} L_v q_{\text{sat}}(\mathbf{T}, \mathbf{p}) + c_p \mathbf{T} + g\mathbf{z}(\mathbf{q}, \mathbf{T}, \mathbf{p}), \quad [13]$$

and we have introduced the dimensionless factor:

$$\kappa(\mathbf{T}, \mathbf{p}) = 1 + \frac{L_v^2 q_{\text{sat}}(\mathbf{T}, \mathbf{p})}{R_v c_p \mathbf{T}^2}. \quad [14]$$

Note that in pressure coordinates, we calculate the geopotential height by vertically integrating the hydrostatic equation after using the ideal gas law:

$$\mathbf{z}(\mathbf{q}, \mathbf{T}, \mathbf{p}) = \int_p^{p_{\text{NS}}} dp' \frac{T(p')}{gp'} \{ R_d + [R_v - R_d] q(p') \}. \quad [15]$$

**B1c. Sensible Heat Fluxes and Surface Pressure.** In this appendix, we discuss the univariate PDFs of the two inputs we did *not* rescale in the main manuscript (see ‘‘Theory’’ Section) in Fig S1 for both super-parameterized models and all three surface temperatures (-4K, +0K, and +4K). The PDF of sensible heat flux changes very little with warming. There is a slight expansion of the left tail of the surface pressure PDF with warming as the most extreme low-pressure systems become more intense, but we hypothesize that these changes are small enough not to require a dedicated input rescaling.

\* not necessarily true close to the surface

## B2. Outputs.

**B2a. Theory.** In contrast to input rescaling, rescaling our ML models' outputs, namely subgrid thermodynamics, only marginally improves the models' ability to generalize. In the absence of physical theory on how the full vertical profile of subgrid thermodynamics changes with warming, we place ourselves in an idealized scenario:

Assuming we know how the outputs' univariate PDF changes with warming, can we help our ML models generalize via output rescaling?

We note that assuming knowledge of how the *univariate* PDFs (or equivalently the CDF) of convective heating and moistening change with warming is more realistic than assuming full knowledge of how their *joint* PDFs change with warming. This knowledge could come from e.g. convection theory (e.g., 12) or shorter simulations than those required to train a subgrid closure. Under this assumption, a natural rescaling is the outputs' cumulative distribution function (CDF):

$$\tilde{\mathbf{y}} = \text{CDF}(\mathbf{y}). \quad [16]$$

In essence, we are assuming that the mapping is more likely to be invariant in quantile than in physical space, which is a common practice when debiasing the outputs of climate models referred to as *quantile mapping* (e.g., review by 13). In practice, we test two distinct methods for rescaling the outputs using their CDFs and report the results for SPCAM3 aquaplanet simulations in SI B2b.

**Quantile mapping after training** The first method is to rescale the ML model's input *during* training, and then rescale the ML model's output *after* training. This is akin to standard, post-hoc, quantile mapping. In the particular case of trying to generalize from a (-4K) cold simulation to a (+4K) warm simulation, the entire transformation to yield outputs in physical units can be mathematically written as:

$$\mathbf{y} \mapsto \text{CDF}_{+4\text{K}}^{-1} [\text{CDF}_{-4\text{K}}(\mathbf{y})], \quad [17]$$

where for simplicity but without loss of generality, we have considered a singular input  $\mathbf{y}$  whose CDF is  $\text{CDF}_{-4\text{K}}$  in the (-4K) cold simulation and  $\text{CDF}_{+4\text{K}}$  in the (+4K) warm simulation.

**Quantile mapping before training** The second method is to rescale the ML model's output *before* training. In that case, we directly train the ML model to predict  $\tilde{\mathbf{y}} = \text{CDF}(\mathbf{y})$  as accurately as possible. We then map the output back to physical units using  $\text{CDF}^{-1}$  *after* training.

**B2b. Results.** The two methods to rescale outputs presented above are depicted in Fig S2 and the generalization results presented in Fig S3. Rescaling outputs *after* training slightly improves generalization skill (from an overall  $R^2$  of 0.58 to 0.62 for the generalization (+4K) set). In contrast, rescaling outputs *before* training leads to equally bad results both on the training and generalization sets, which is a negative result underlining the challenges of designing the appropriate loss function in quantile space. A possible solution would be to convert back the outputs to physical space before feeding them to the loss function during training, and further investigation is required to fully assess the potential and limitations of training these ML models in quantile space.

**B3. Coordinate** . Another rescaling to consider when input/output variables are functions of spatiotemporal coordinates is *coordinate rescaling*, resulting in a coordinate change. In our specific example, it is possible to rescale the vertical coordinate, i.e. the hybrid pressure coordinate  $p$ . Possible rescalings include:

1. the temperature ( $\tilde{p} = T$ ), e.g. for radiative heating, which tends to vary less in temperature coordinates (14),
2. the saturation specific humidity ( $\tilde{p} = q_{\text{sat}}$ ) which is consistent with a transformation of the primitive equations that captures an upward shift of the circulation as the climate warms (15),
3. the geopotential height or the altitude ( $\tilde{p} = z$ ), which could more consistently capture gravity wave propagation,
4. or a coordinate with fixed values for characteristic vertical levels in the atmosphere, such as the top of the planetary boundary layer or the tropopause (16).

While we were able to rescale the vertical coordinate using interpolation functions (not shown), the benefits were not visible in our particular case. This could be because input rescaling already addresses the upward shift of convective activity warming, as shown in Fig 8 and Fig S11.

### C. Implementation

For reproducibility purposes (17), we now detail the practical implementation of a “climate-invariant” ML workflow (see Fig S4), from its overall structure (SI C1) to its benchmarking (SI C4) via the characteristics of the multiple linear regressions (MLR, SI C2) and neural networks (NN, SI C3) presented in this manuscript.

**C1. Overall Workflow.** We present three ways to implement physical rescalings. The first way is to physically rescale the inputs/outputs *before* training (see code at [link]). While this option is easiest to implement and debug, it usually comes at the cost of disk space: Every time we try a new rescaling, we need to duplicate our training/validation/test datasets for all the climates/geographies we are interested in, which can quickly be prohibitive when trying multiple rescaling combinations.

Therefore, it can be advantageous to rescale the input/output variables within the ML framework, so that the rescalings occur *during* training. In essence, we are trading disk space for computational time. In that spirit, the second method is to rescale the inputs/outputs via custom layers (e.g., Ch 12 of 18) in the ML algorithm itself (see code at [link]). Since this second method tends to substantially slow down training as it adds sequential operations on the GPU, we take advantage of the fact that the rescalings occur before and after the emulated mapping, and propose a third method that can happen in parallel on the CPU: Rescaling inputs/outputs by customizing the pipeline or “data generator” (see code at [link]), which is the algorithm responsible for feeding numbers to the ML model after reading the training data files. For each batch, the *custom data generator* then rescales inputs *before* feeding them to the ML algorithm. In our case, note that we rescale outputs independently via quantile mapping (see SI B2).

For the rest of this manuscript, we will train our ML models using custom data generators: For “brute-force” models, the rescalings are set to None (no rescaling), while for “climate-invariant” models, the  $q$  rescaling is set to  $\tilde{q}_{\text{RH}}$ , the  $T$  rescaling is set to  $\tilde{T}_{\text{buoyancy}}$ , and the LHF rescaling is set to  $\tilde{\text{LHF}}_{\Delta q}$ . For all models, we additionally subtract the mean from each input before dividing it by its range to feed the ML algorithm floating-point numbers between (-1) and 1. Note that for each rescaling, numbers are “de-normalized” before the rescaling and “re-normalized” after, so that all rescalings are done in physical units while the ML algorithm is always fed single-precision floating-point numbers in  $[-1, 1]$ .

For simplicity and building upon previous ML-powered subgrid closures (4, 6, 19), we use the mean-squared error (MSE) of the prediction *in physical units* (here  $\text{W}^2\text{m}^{-4}$ ) as our loss function. Motivated by the framework presented in Fig 3, we first train MLRs (SI C2) before training NNs (SI C3) and benchmarking our ML models to quantify their accuracy and ability to generalize (SI C4).

**C2. Multiple Linear Regressions.** To use the same data generator for both MLRs and NNs, we implement our MLRs in Tensorflow 2.0 (20) and train them using the Adam optimizer (21), which builds on stochastic gradient descent (22). Training a “climate-invariant” MLR results in a weight matrix  $\mathbf{A}$  of size  $4N_p \times (2N_p + 4)$  and a bias vector  $\mathbf{b}$  of length  $4N_p$  such that:

$$\mathbf{y} \approx \mathbf{A}\tilde{\mathbf{x}} + \mathbf{b}, \quad [18]$$

where stochastic optimization means that there is no unique optimal solution for  $\mathbf{A}$  and  $\mathbf{b}$ . We train MLRs for 20 epochs using the Adam optimizer (21) with the default Keras learning rate of 0.001 and save the weights and biases corresponding to the minimal loss over the validation set.

**C3. Neural Networks.** To isolate the effects of physically rescaling the NN’s inputs, we fix the hyperparameters of all NNs trained in this study, and leave the joint investigation of hyperparameter tuning and physical rescalings for future work. Informed by (23) and (24), we fix the architecture to 7 layers of 128 neurons separated by Leaky Rectified Linear Unit activation functions of slope 0.3, resulting in 122,872 trainable parameters for each NN. We implement the SPCAM NNs using Tensorflow 2.0 (20), train them for 20 epochs using the Adam optimizer with the default Keras learning rate of 0.001 and a default batch size of 1024, and save the parameters corresponding to the minimal validation loss.

Following the supplemental material (Sec 2) of (25), some of the hyperparameters used for the NNs trained on SAM data are different. The SAM NNs are implemented using PyTorch 1.4.0 (26), have 5 dense layers of 128 neurons each, and use cyclic learning rate (27): Starting with an initial learning rate in  $[2 \times 10^{-4}, 2 \times 10^{-3}]$  for the first epoch out of 10, we then reduce the minimal and maximal learning rates by 10% for the next 6 epochs before further reducing them by a factor 10 for the last 3 epochs.

For SPCAM and following (28), we augment some of our NNs with BN and DP layers, more specifically one DP layer before each activation function and a single BN layer before the first DP layer. Following (29), we use the default DP rate of 30% and the default parameters of the Keras BN layer that



normalize each feature using its mean and standard deviation in a given batch (30). Note that we do not adjust the default parameters of DP and BN to optimize *generalization* skill as this would require misusing the generalization test set as a validation test.

**C4. Benchmarking.** We benchmark our ML models using two different metrics: their MSEs and their coefficient of determination  $R^2$ , defined for a singular output  $y_k$  as:

$$R^2 \stackrel{\text{def}}{=} 1 - \frac{\langle y_{\text{Err},k}^2 \rangle_{\text{samp}}}{\langle (y_{\text{Truth},k} - \langle y_{\text{Truth},k} \rangle_{\text{samp}})^2 \rangle_{\text{samp}}}, \quad [19]$$

where  $\langle \cdot \rangle_{\text{samp}}$  is the averaging operator over the samples of interest. For instance, if we want a horizontal map of  $R^2$ , we average samples at a given location over time, while we average over time and horizontal space if we want a single  $R^2$  value for  $y_k$ . Similarly, if we want one value of MSE per output  $y_k$ , we only average the MSE over time and horizontal space rather than over all outputs, as when calculating the loss function.

While comparing MSE and  $R^2$  in the reference and target generalization climates is enough to assess generalization skill *after* training, we are also interested in how a given ML model learns to generalize *during* training. To address that question, we augment our SPCAM ML models with a function (technically a “Keras callback” (31)) that calculates the MSE over two datasets that correspond to the two generalization experiments at the end of each epoch: (1) a dataset of different temperature (warm when training on cold, and vice-versa); and (2) a dataset of different geography (Earth-like when training on Aquaplanet, and vice-versa). At the end of training, we hence obtain three learning curves for each ML model: the validation loss, and the loss in the two generalization sets as a function of number of epochs. Note that these callbacks are computationally expensive as they require evaluating the ML model over  $\approx 100M$  samples at the end of each epoch, which means they should be avoided when purely seeking performance, e.g. during hyperparameter tuning.

## D. Supplementary Results

**D1. Jensen-Shannon Distance between PDFs across Climates.** As an alternative to the Hellinger PDF distance, we pick the Jensen-Shannon distance (32) because it is a symmetric distance (i.e., the arguments’ order does not affect the outcome) that uses the logarithms of the PDFs, hence giving large weights to the PDFs’ tails that tend to be particularly problematic for generalization purposes:

$$\text{JS}(p, q) \stackrel{\text{def}}{=} \sqrt{\frac{1}{2} [\text{KL}(p, q) + \text{KL}(q, p)]}, \quad [20]$$

where  $p$  and  $q$  are the normalized PDFs to compare and KL is the Kullback–Leibler divergence, defined for continuous PDFs as:

$$\text{KL}(p, q) \stackrel{\text{def}}{=} \int_0^1 dx \times p(x) \ln \left[ \frac{p(x)}{q(x)} \right]. \quad [21]$$

**D2. Learning across Climates and Geographies.** This section complements the main text and shows that “climate-invariant” models learn mappings that are valid across climates and geographies *during* training.

Fig S5 shows learning curves; the color of each line indicates the dataset the model was *trained* in, while the color of the row indicates the dataset the model was *tested* in. To gain intuition, we can start by looking at lines that have the same color as their boxes: These are the “standard” learning curve showing that each model’s validation loss in the same climate/geography monotonically decreases as the model is trained, confirming that we are not overfitting the training set.

We are now ready to zoom in on a key result of this manuscript: The learning curve of the “climate-invariant” NN trained in the cold aquaplanet but tested in the warm aquaplanet (starred blue line in the red box (a)). Impressively, this learning curve is mostly decreasing, confirming that “*climate-invariant*” NNs are able to continuously learn about subgrid thermodynamics in the warm aquaplanet as they are trained in the cold aquaplanet. In contrast, the “brute-force” NN trained in the cold aquaplanet but tested in the warm aquaplanet (circled blue line in the red box (a)) makes extremely large generalization errors, which worsen as the model is trained in the cold aquaplanet.

“*Climate-invariant*” NNs also facilitate learning across geographies, i.e., from the aquaplanet to the Earth-like simulations (starred blue line in green box (b) is consistently below circled blue line) and vice-versa (starred green line in blue box (c) is consistently below circled green line). “Climate-invariant” rescalings additionally improve the MLR baseline’s generalization ability (see right column, e.g., starred blue line in red box (a) and starred green line in blue box (c)), albeit less dramatically. This smaller improvement in MLR’s generalization abilities is linked to its relatively small number of free parameters, resulting in (1) “brute-force” MLRs generalizing better than “brute-force” NNs; and (2) MLRs having lower representation power and fitting their training sets less well, limiting the maximal accuracy of “climate-invariant” MLRs on the test set.

There are a few cases in which rescaling inputs does not fully solve the generalization problem, e.g., when trying to generalize from the aquaplanet to the Earth-like simulation (starred blue line in green box (b)). NNs with DP fit their training set less well (squared lines that have the same color as their boxes are above corresponding circled/starred lines). However, they improve generalization in difficult cases (e.g., squared blue line in green box (b)) and do not overly deteriorate generalization in cases where the input rescalings work particularly well (e.g., squared green line in blue box (a)). This confirms that *combining physics-guided generalization methods* (e.g., *physical rescaling of the inputs/outputs*) with *standard ML generalization methods* (e.g., *DP*) is advantageous.

**D3. Geographical Skill.** To show that the improved generalization skill of “climate-invariant” NNs for subgrid heating is not unique to the mid-troposphere, we show the generalization skill of “climate-invariant” NNs near the surface in Fig S6

Consistently with (24, 33), the highest skill for the training climate is over land for all NNs as most of the variability comes from the diurnal cycle, which is easy to predict for NNs. Similarly to Fig 8, the generalization error is apparent for the brute-force NN (a) and mostly solved by making the NN

climate-invariant (b).

**D4. Visualizing Climate-Invariant Mappings.** Before using SHAP in the “Results” Section to visualize the difference between brute-force and climate-invariant mappings, we test simple linear methods to analyze ML models. First, we directly plot the weights  $\mathbf{A}$  (see Eq 18) of our multi-linear regressions in Fig S7. Second, we plot the mean Jacobian of our NN calculated via automatic differentiation in Fig S9. Unlike SHAP, the MLR weights and the Jacobian matrices both suggest that the climate-invariant mapping is non-local in the vertical. Fig S7 is consistent with the climate-invariant MLR generalizing only slightly better than the brute-force MLR (see top-right panel of Fig S5). Meanwhile, comparing Fig S9 to the full SHAP feature importance matrix (Fig S11) suggests that while the linear sensitivity of subgrid heating/moistening with respect to lower-tropospheric plume buoyancy is high (top panels of Fig S9b), which is expected, subgrid heating/moistening can be well-predicted using mostly local plume buoyancy information (top panels of Fig S11b).

Model	Spatiotemporal Resolution	Training Set	Validation Set	Test Set
SPCAM3	$(2.8^\circ \times 2.8^\circ)_{T42} \times 30\text{lev} \times 30\text{min}$	Yr2, Mo1-4 $\rightarrow$ 47M	Yr2, Mo5-8 $\rightarrow$ 48M	Yr1, Mo6-9 $\rightarrow$ 48M
SPCAM5	$2.5^\circ \times 1.9^\circ \times 30\text{lev} \times 15\text{min}$	Yr1, Day0-9/Mo $\rightarrow$ 143M	Yr2, Day0-9/Mo $\rightarrow$ 143M	Yr2, Day20-28/Mo $\rightarrow$ 118M
SAM (-4K) (+0K)	96km $\times$ 96km $\times$ 48lev $\times$ 180min	day 225-545 $\rightarrow$ 13.8M	day 545-562 $\rightarrow$ 0.7M	day 562-587 $\rightarrow$ 2.6M
	96km $\times$ 96km $\times$ 48lev $\times$ 180min	-	-	day 380-405 $\rightarrow$ 2.6M

**Table S1. Characteristics of the training/validation/test sets used in this manuscript. The spatiotemporal resolution uses the format longitude  $\times$  latitude  $\times$  vertical levels  $\times$  time. For SPCAM3, which uses a T42 spectral truncation, we use months 1 to 4 of the second simulation year to build the training set, resulting in  $\approx 47M$  samples. For SPCAM5, we use the first 9 days of every month of the first simulation year to build the training set, resulting in  $\approx 143M$  samples.**

Row	Input	SPCAM3	SPCAM5	SAM
1	$q_{600\text{hPa}}$	0.5, <b>0.8</b>	0.4, <b>0.7</b>	0.5
2	$q_{\text{deficit}, 600\text{hPa}}$	0.7, <b>1.0</b>	0.4, <b>0.8</b>	0.8
3	$\text{RH}_{600\text{hPa}}$	0.1, <b>0.2</b>	0.1, <b>0.1</b>	0.1
4	$T_{850\text{hPa}}$	1.4, <b>1.9</b>	0.5, <b>0.8</b>	1.3
5	$T_{\text{from NS}, 850\text{hPa}}$	0.1, <b>0.1</b>	0.1, <b>0.1</b>	0.2
6	$B_{\text{plume}, 850\text{hPa}}$	0.2, <b>0.3</b>	0.1, <b>0.2</b>	0.1
7	$T_{150\text{hPa}}$	0.6, <b>0.7</b>	0.7, <b>0.7</b>	1.5
8	$T_{\text{from NS}, 150\text{hPa}}$	0.9, <b>1.4</b>	0.3, <b>0.6</b>	1.4
9	$B_{\text{plume}, 150\text{hPa}}$	1.0, <b>1.2</b>	0.2, <b>0.4</b>	0.5
10	LHF	0.2, <b>0.3</b>	0.2, <b>0.3</b>	
11	$\text{LHF}_q$	0.1, <b>0.2</b>	0.2, <b>0.2</b>	
12	$\text{LHF}_{\Delta q}$	0.1, <b>0.2</b>	0.2, <b>0.3</b>	

**Table S2. Jensen-Shannon distance away from the (-4K) simulation for the PDFs of ( $q_{600\text{hPa}}$ ,  $T_{850\text{hPa}}$ ,  $T_{150\text{hPa}}$ , LHF) and their rescalings: (+0K) distance in gray and (+4K) distance in red.**

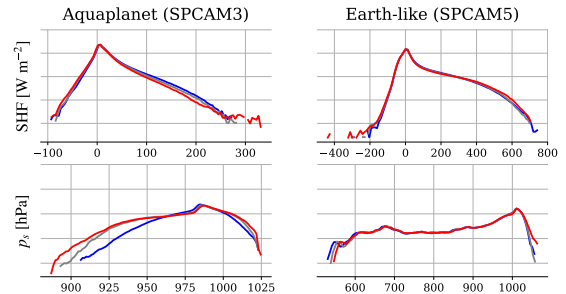


**Fig. S1. Univariate PDFs of the sensible heat flux and surface pressure in the cold (blue), reference (gray), and warm (red) simulations of SPCAM3 and SPCAM5. For a given variable, we use the same vertical logarithmic scale across models.**

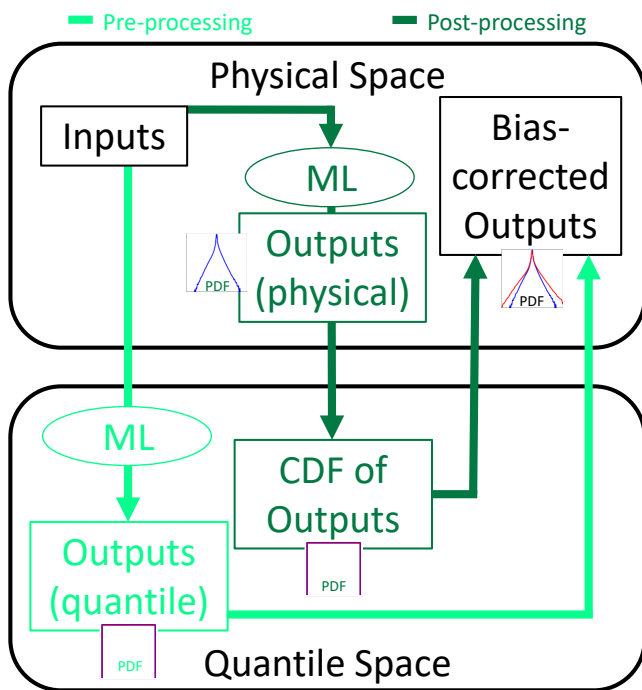


**Fig. S2.** Two types of bias-correction methods used to rescale outputs in SI B2: (dark green, "post-processing" method) Quantile mapping is typically done *after* training the model to bias-correct the outputs, and (light green, "pre-processing" method) we additionally test directly making predictions in quantile space by converting the outputs to quantiles *before* training. Note that this usually changes the loss function.

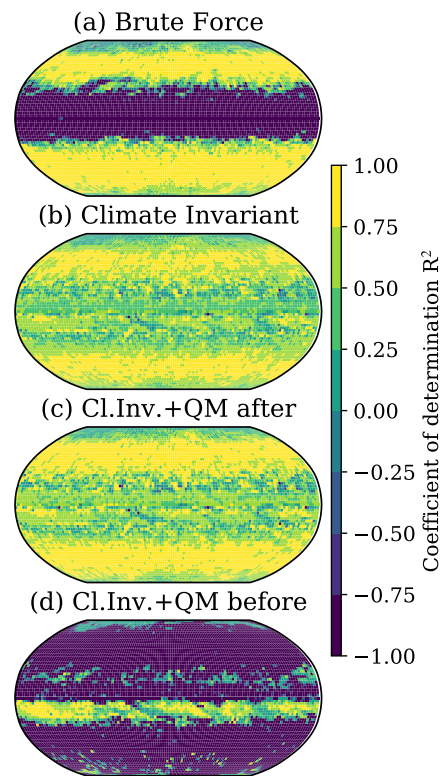


**Fig. S3.** Coefficient of determination  $R^2$  for 500-hPa subgrid heating of brute-force (a), climate-invariant (b), climate-invariant with outputs rescaled *after* training (c), climate-invariant with outputs rescaled *before* training (d) NNs trained using the cold (-4K) training set of SPCAM3 and calculated over the warm (+4K) training set of SPCAM3.



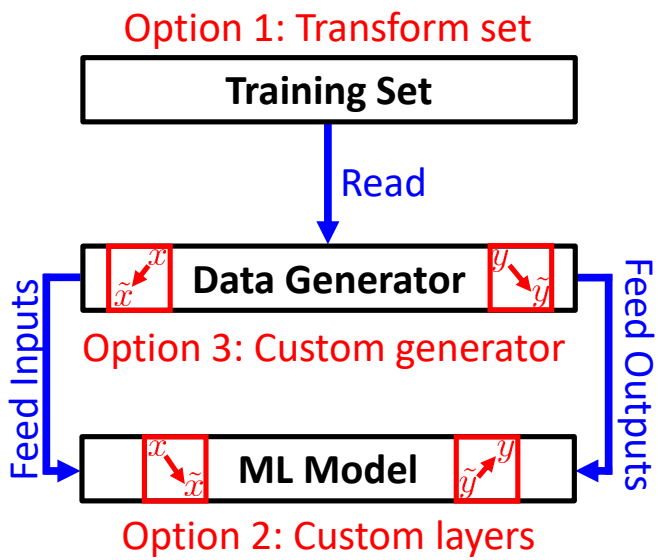


**Fig. S4.** Implementation of the climate-invariant ML framework: The physical rescalings can be implemented by (Option 1) transforming the training set, (Option 2) adding custom layers to the ML model, or (Option 3) customizing the data generator so that it automatically transforms the model inputs/outputs.

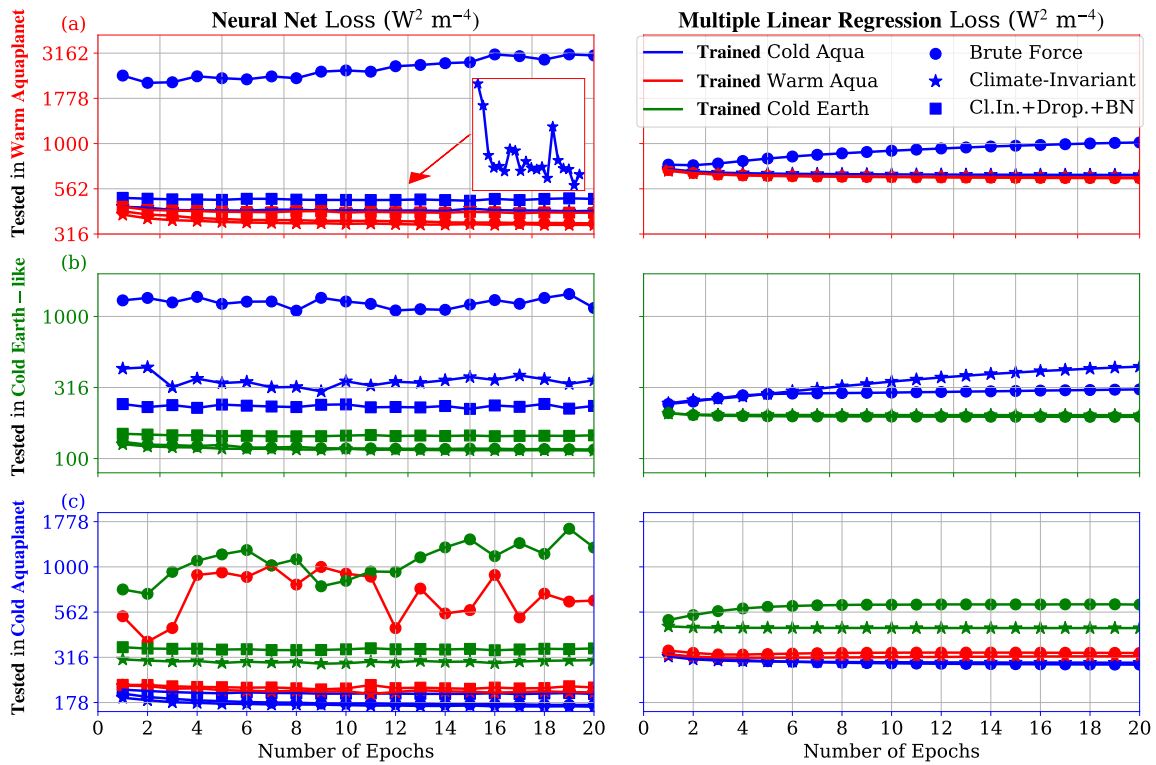


**Fig. S5.** Learning curves of neural nets (left) and multiple linear regressions (right) tested in the (-4K) cold aquaplanet simulation (a, top row), the (+4K) warm aquaplanet simulation (b, middle row), and the (-4K) cold Earth-like simulation (c, bottom row). The lines' colors indicate the **training** dataset, while their symbols refer to whether the ML model is brute-force (circle), climate-invariant (star), or climate-invariant with dropout layers before each activation function and batch normalization (square). (b) We additionally zoom in on the climate-invariant neural network's learning curve in the (+4K) simulation.

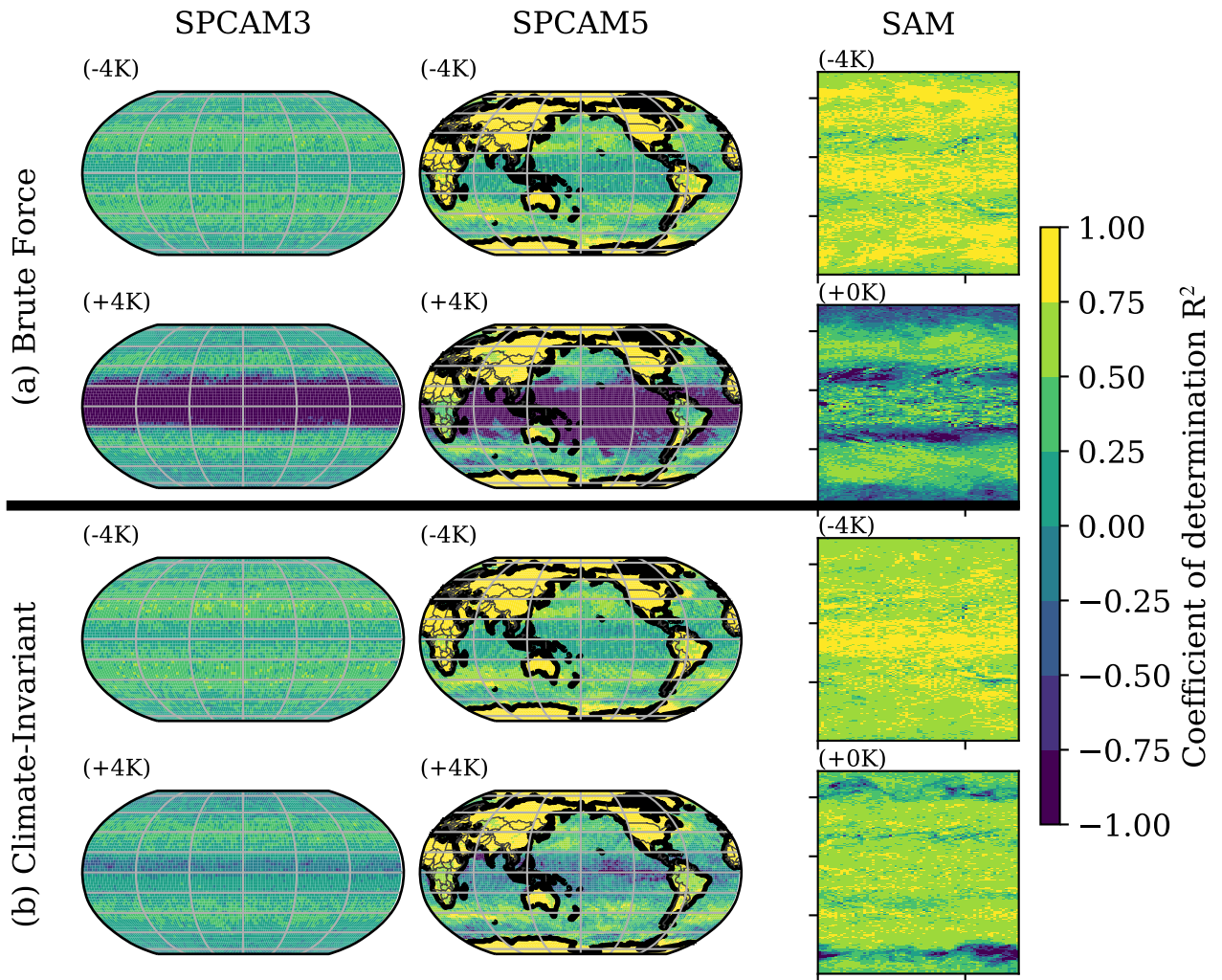
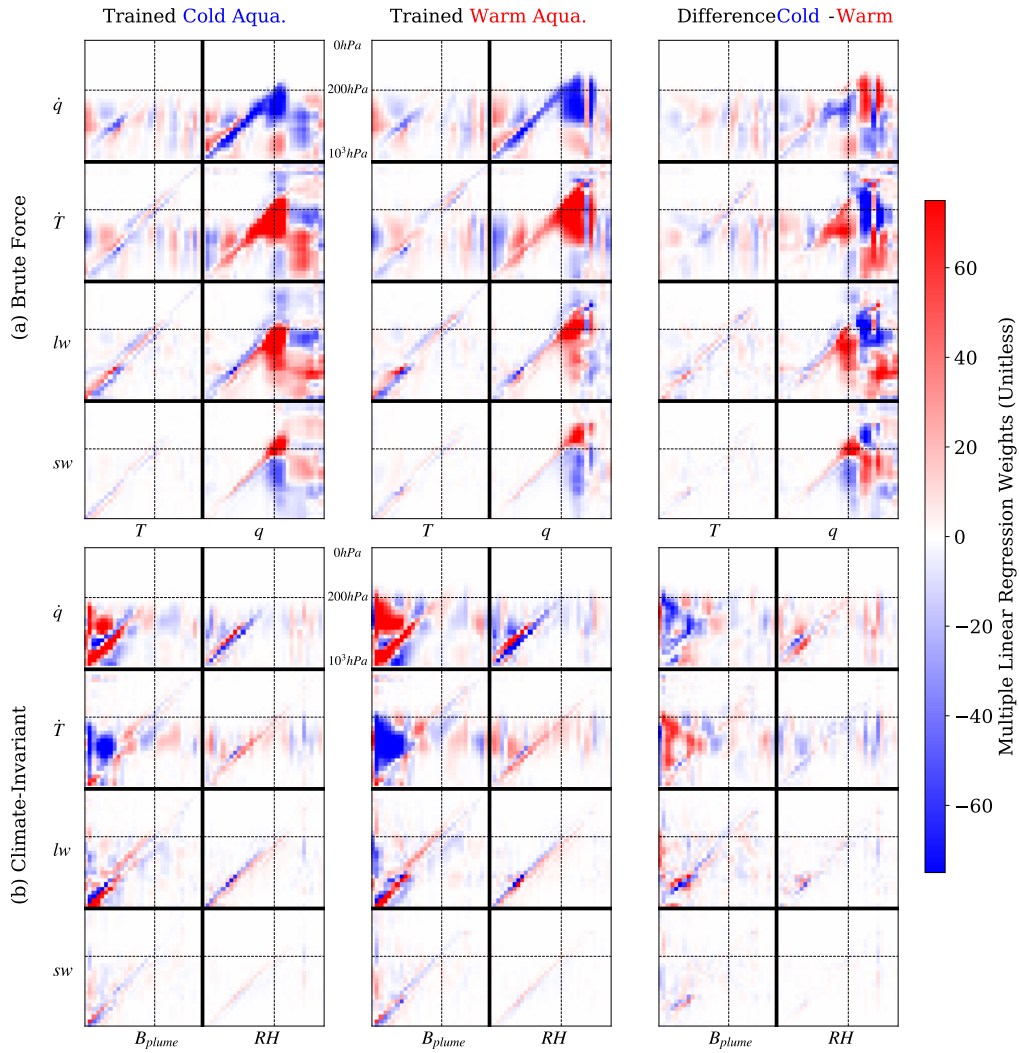
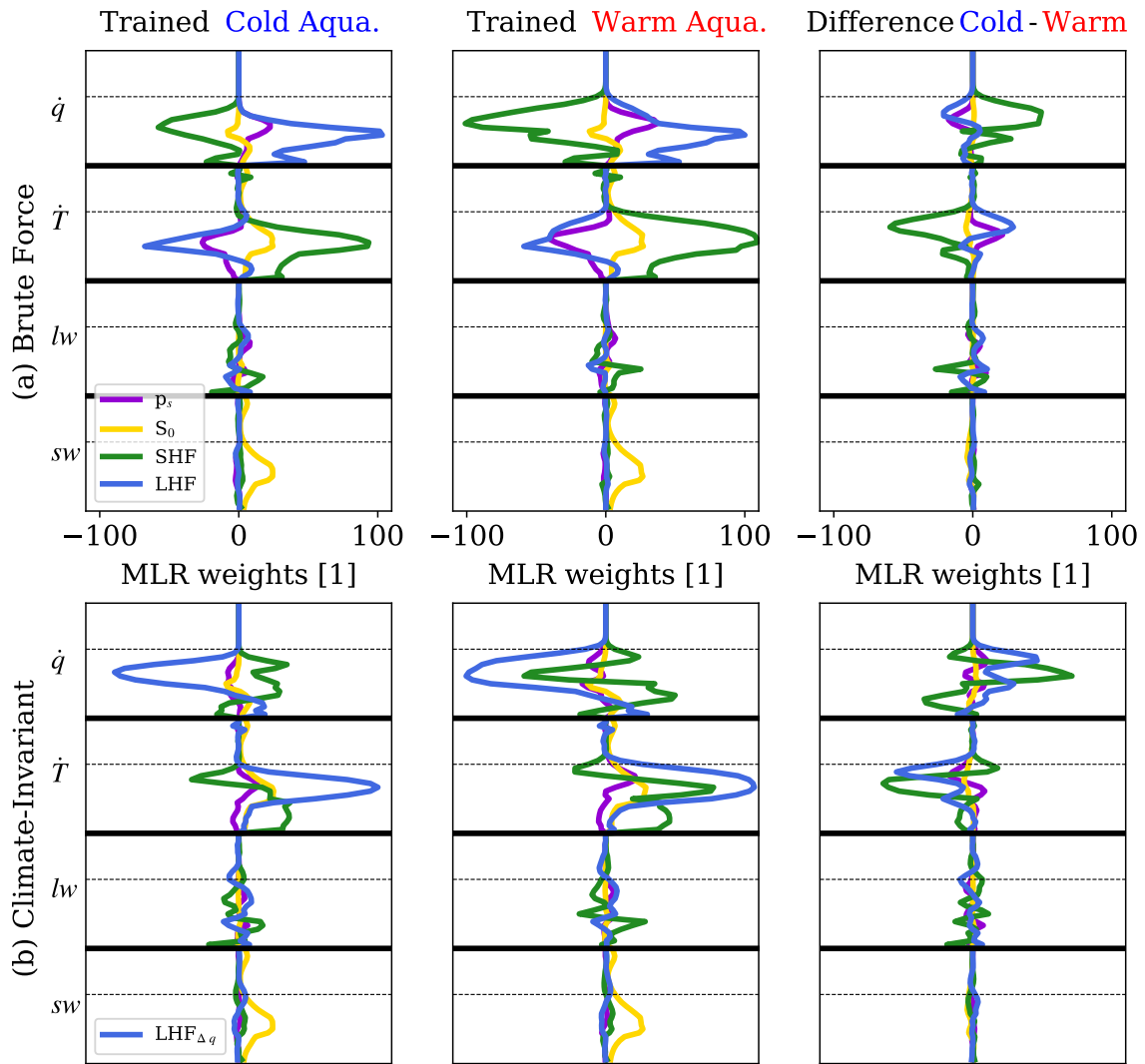


Fig. S6. Same as Fig 6 for near-surface subgrid heating.



**Fig. S7.** Weights of the (a) brute-force and (b) climate-invariant multi-linear regressions trained in the cold (-4K) aquaplanet simulation (left), the warm (+4) warm aquaplanet simulation (middle), and their difference (right). The x-axes indicate the vertical levels of the inputs, from the surface (left,  $10^3$  hPa) to the top of the atmosphere (right, 0 hPa), while the y-axes indicate the vertical levels of the outputs, from the surface (bottom,  $10^3$  hPa) to the top of the atmosphere (top, 0 hPa). We additionally indicate the 200 hPa vertical level with dotted black lines.





**Fig. S8.** Same as Fig S7, but for the four scalar inputs used in addition to the temperature and specific humidity inputs: Surface pressure ( $p_s$ , purple line), solar insolation ( $S_0$ , yellow line), surface sensible heat flux (SHF, green line), and surface latent heat flux (LHF, blue line). For the climate-invariant mapping (b), LHF is rescaled to  $LHF_{\Delta q}$  as described in the "Theory" section, which in conjunction with the temperature and humidity rescalings, changes the multi-linear regression weights for all input variables.

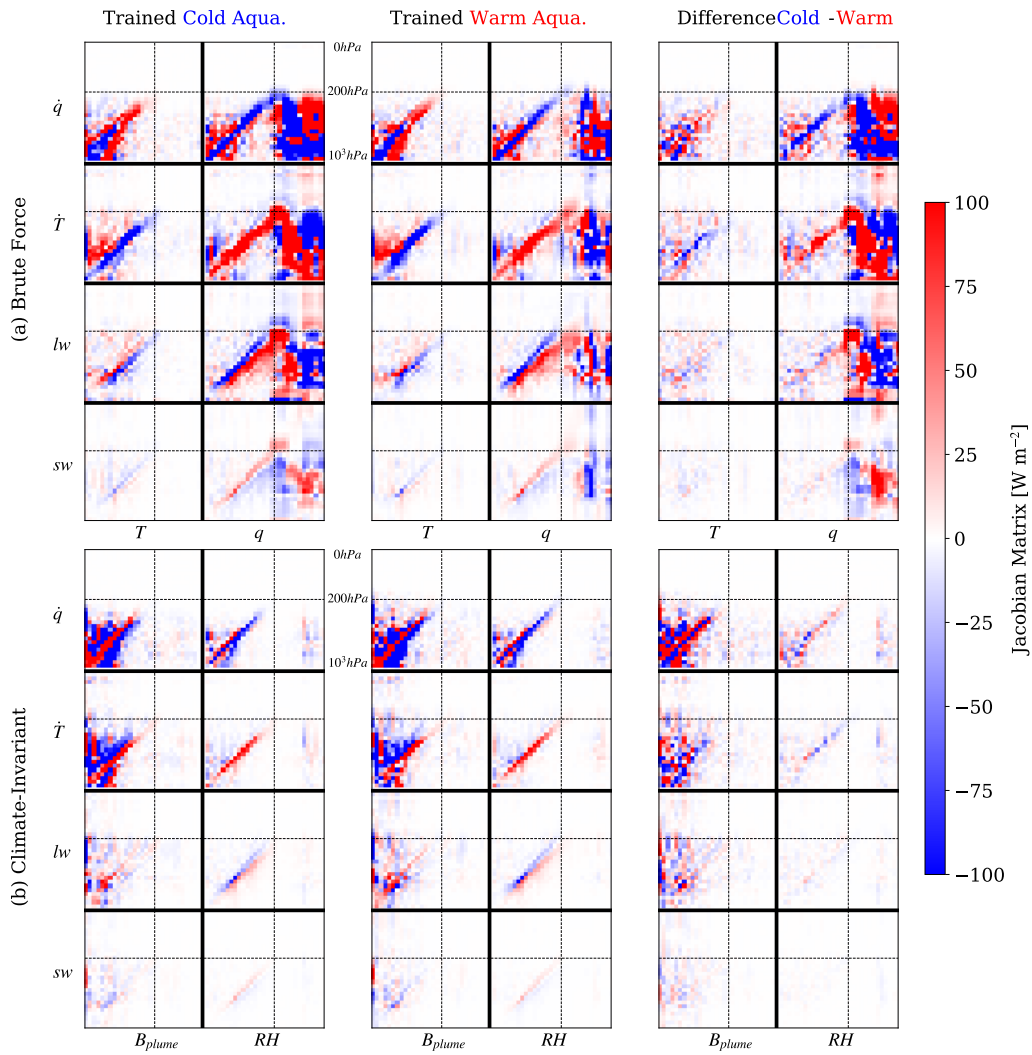


Fig. S9. Same as Fig S7 for the Jacobian matrices.

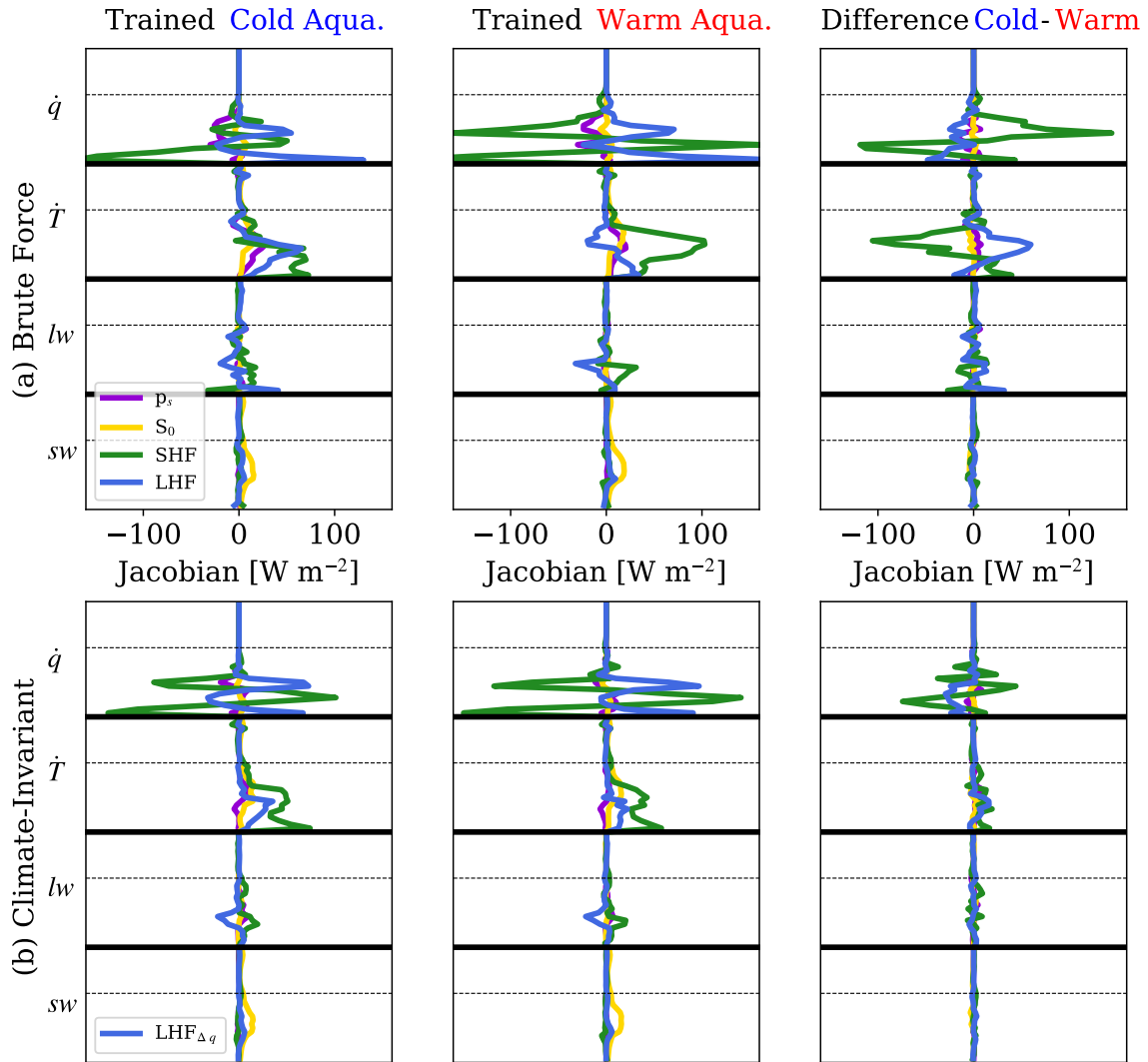
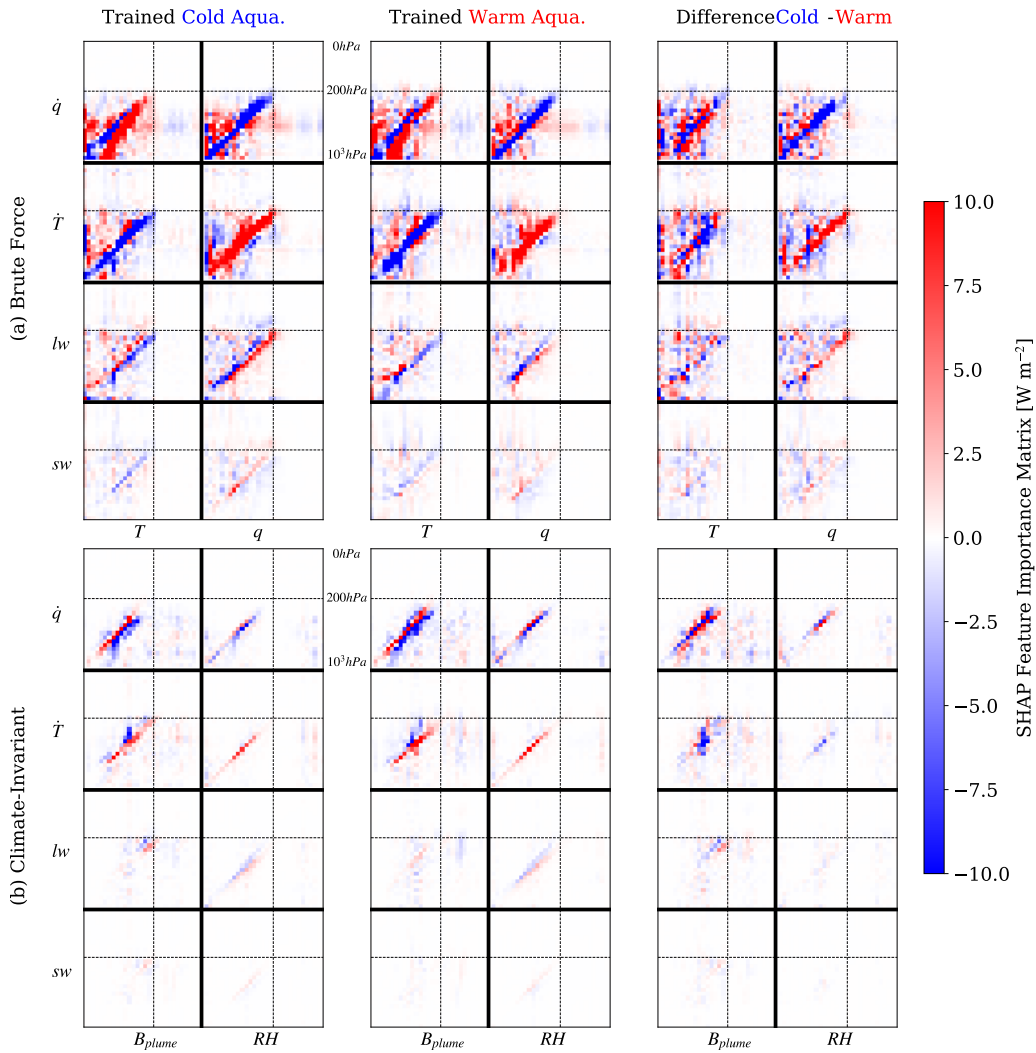
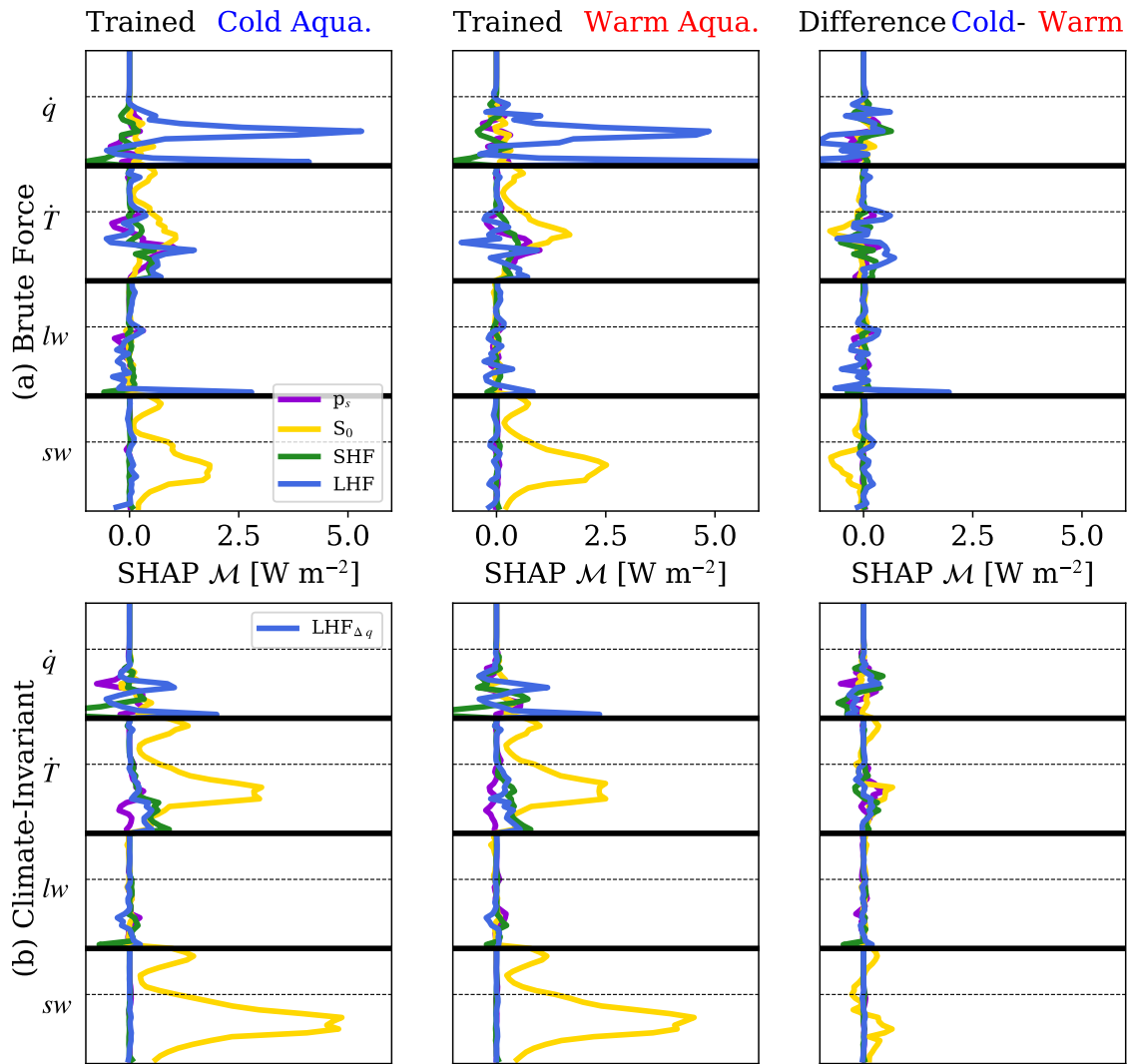


Fig. S10. Same as Fig S8 for the Jacobian.



**Fig. S11.** SHAP feature importance matrix for the (a) brute-force and (b) climate-invariant neural nets trained in the cold (-4K) aquaplanet simulation (left), the warm (+4) warm aquaplanet simulation (middle), and their difference (right). To calculate these matrices, we sample inputs from the (+4K) warm aquaplanet simulation for all ML models to facilitate inter-model comparison. The x-axes indicate the vertical levels of the inputs, from the surface (left, 10<sup>3</sup>hPa) to the top of the atmosphere (right, 0hPa), while the y-axes indicate the vertical levels of the outputs, from the surface (bottom, 10<sup>3</sup>hPa) to the top of the atmosphere (top, 0hPa). We additionally indicate the 200hPa vertical level with dotted black lines.





**Fig. S12.** Same as Fig S11, but for the four scalar inputs used in addition to the temperature and specific humidity inputs: Surface pressure ( $p_s$ , purple line), solar insolation ( $S_0$ , yellow line), surface sensible heat flux (SHF, green line), and surface latent heat flux (LHF, blue line). For the climate-invariant mapping (b), LHF is rescaled to  $LHF_{\Delta q}$  as described in the “Theory” section, which in conjunction with the temperature and humidity rescalings, changes the SHAP feature importance matrix for all input variables.

## References

1. S Rasp, T Beucler, G Reinaudi, P Gentine, tbeucler/cbrain-cam: Climate\_invariant\_ml (2021).
2. T Beucler, M Pritchard, L Peng, J Yuval, Climate-invariant machine learning (2021).
3. S Rasp, raspstephan/cbrain-cam (2018).
4. S Rasp, MS Pritchard, P Gentine, Deep learning to represent subgrid processes in climate models. *Proc. Natl. Acad. Sci.* **115**, 9684–9689 (2018).
5. H Parishani, et al., Insensitivity of the cloud response to surface warming under radical changes to boundary layer turbulence and cloud microphysics: Results from the ultraparameterized cam. *J. Adv. Model. Earth Syst.* **10**, 3139–3158 (2018).
6. J Yuval, PA O’Gorman, Stable machine-learning parameterization of subgrid processes for climate modeling at a range of resolutions. *Nat. communications* **11**, 1–10 (2020).
7. J Yuval, yanyuval/Neural\_network\_parameterization: Associated code and data for “Use of neural networks for stable, accurate and physically consistent parameterization of subgrid atmospheric processes with good performance at reduced precision” (2020).
8. MF Khairoutdinov, DA Randall, Cloud resolving modeling of the arm summer 1997 iop: Model formulation, results, uncertainties, and sensitivities. *J. Atmospheric Sci.* **60**, 607–625 (2003).
9. KA Emanuel, et al., *Atmospheric convection*. (Oxford University Press on Demand), (1994).
10. F Ahmed, ÁF Adames, JD Neelin, Deep convective adjustment of temperature and moisture. *J. Atmospheric Sci.* **77**, 2163–2186 (2020).
11. AF Adames, SW Powell, F Ahmed, VC Mayta, JD Neelin, Tropical precipitation evolution in a buoyancy-budget framework. *J. Atmospheric Sci.* **78**, 509 – 528 (2021).
12. AP Siebesma, S Bony, C Jakob, B Stevens, *Clouds and Climate: Climate Science’s Greatest Challenge*. (Cambridge University Press), (2020).
13. D Maraun, Bias correcting climate change simulations—a critical review. *Curr. Clim. Chang. Reports* **2**, 211–220 (2016).
14. N Jeevanjee, DM Romps, Mean precipitation change from a deepening troposphere. *Proc. Natl. Acad. Sci.* **115**, 11465–11470 (2018).
15. MS Singh, PA O’Gorman, Upward shift of the atmospheric general circulation under global warming: Theory and simulations. *J. climate* **25**, 8259–8276 (2012).
16. JT Seeley, N Jeevanjee, DM Romps, Fat or fitt: Are anvil clouds or the tropopause temperature invariant? *Geophys. Res. Lett.* **46**, 1842–1850 (2019).
17. D Irving, A minimum standard for publishing computational results in the weather and climate sciences. *Bull. Am. Meteorol. Soc.* **97**, 1149–1158 (2016).
18. A Géron, *Hands-on machine learning with Scikit-Learn, Keras, and TensorFlow: Concepts, tools, and techniques to build intelligent systems*. (O’Reilly Media), (2019).
19. ND Brenowitz, CS Bretherton, Spatially extended tests of a neural network parametrization trained by coarse-graining. *J. Adv. Model. Earth Syst.* **11**, 2728–2744 (2019).
20. M Abadi, et al., TensorFlow: Large-scale machine learning on heterogeneous systems (2015) Software available from tensorflow.org.
21. DP Kingma, J Ba, Adam: A method for stochastic optimization. *arXiv preprint arXiv:1412.6980* (2014).
22. J Kiefer, J Wolfowitz, Stochastic estimation of the maximum of a regression function. *The Annals Math. Stat.* pp. 462–466 (1952).
23. J Ott, et al., A fortran-keras deep learning bridge for scientific computing. *Sci. Program.* **2020** (2020).
24. G Mooers, et al., Assessing the potential of deep learning for emulating cloud superparameterization in climate models with real-geography boundary conditions. *J. Adv. Model. Earth Syst.* **13**, e2020MS002385 (2021).
25. J Yuval, PA O’Gorman, CN Hill, Use of neural networks for stable, accurate and physically consistent parameterization of subgrid atmospheric processes with good performance at reduced precision. *Geophys. Res. Lett.* **48**, e2020GL091363 (2021).
26. A Paszke, et al., Pytorch: An imperative style, high-performance deep learning library in *Advances in Neural Information Processing Systems 32*, eds. H Wallach, et al. (Curran Associates, Inc.), pp. 8024–8035 (2019).
27. LN Smith, Cyclical learning rates for training neural networks in *2017 IEEE Winter Conference on Applications of Computer Vision (WACV)*. (IEEE), pp. 464–472 (2017).
28. MJ Molina, DJ Gagne, AF Prein, A benchmark to test generalization capabilities of deep learning methods to classify severe convective storms in a changing climate. *Earth Space Sci. Open Arch. ESSOAr* (2021).
29. N Srivastava, G Hinton, A Krizhevsky, I Sutskever, R Salakhutdinov, Dropout: a simple way to prevent neural networks from overfitting. *The journal machine learning research* **15**, 1929–1958 (2014).
30. S Ioffe, C Szegedy, Batch normalization: Accelerating deep network training by reducing internal covariate shift in *International conference on machine learning*. (PMLR), pp. 448–456 (2015).
31. F Chollet, et al., Keras: The python deep learning library. *Astrophys. Source Code Libr.* pp. ascl-1806 (2018).
32. DM Endres, JE Schindelin, A new metric for probability distributions. *IEEE Transactions on Inf. theory* **49**, 1858–1860 (2003).
33. Y Han, GJ Zhang, X Huang, Y Wang, A moist physics parameterization based on deep learning. *J. Adv. Model. Earth Syst.* **12**, e2020MS002076 (2020).